POLITECNICO DI TORINO
Repository ISTITUZIONALE

A low-cost and non-refractory high-entropy alloy for biomedical applications

Original
A low-cost and non-refractory high-entropy alloy for biomedical applications / Muro Torrento, J.E., Sousa, T.D.S.P.D., Moreira Afonso, C.R., Santos De Almeida, G., Zambuzzi, W.F., Corrêa, M.R., Fosca, M., Rau, J.V., Spriano, S., Ubertalli, G., Ghiara, G., Fonzar Pintão, C.A., Grandini, C.R., Nespeque Correa, D.R.. - In: CELL REPORTS PHYSICAL SCIENCE. - ISSN 2666-3864. - 7:10(2026), pp. 1-20. [10.1016/j.xcrp.2026.103547]

Availability:
This version is available at: 11583/3017411 since: 2026-11-02T14:45:02Z

Publisher:
Elsevier

Published
DOI:10.1016/j.xcrp.2026.103547

Terms of use:

This article is made available under terms and conditions as specified in the corresponding bibliographic description in the repository

Publisher copyright

(Article begins on next page)

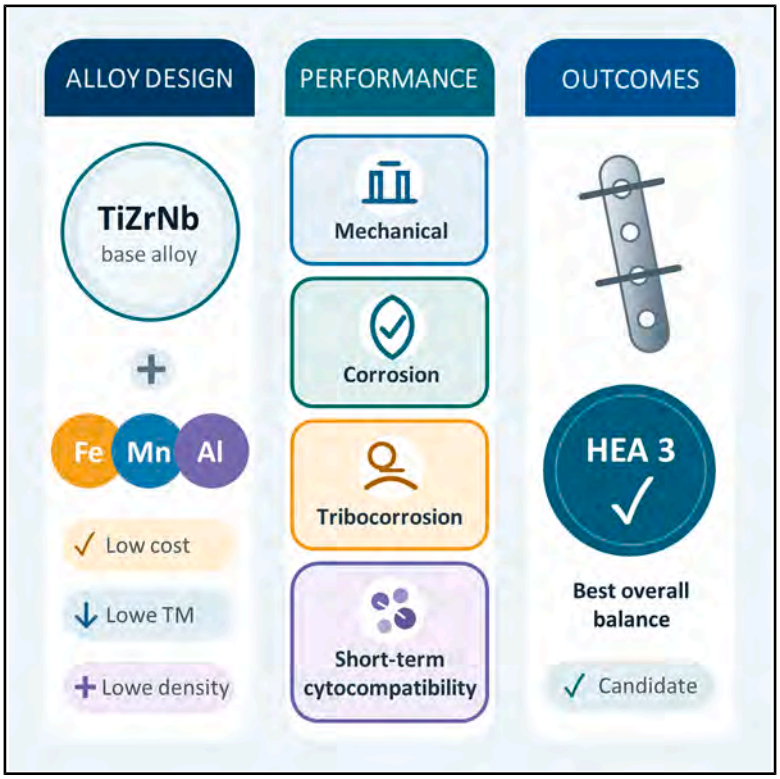
19 November 2026

Cell Reports
Physical Science

Article

A low-cost and non-refractory high-entropy alloy for biomedical applications

Graphical abstract



Highlights

- Low-cost elements enable high-entropy alloys with lower melting points
- The alloys combine approximately 420 HV hardness with 90–100 GPa elastic modulus
- Stable passive films provide corrosion resistance comparable to Ti-6Al-4V
- HEAs show enhanced tribocorrosion resistance and support cell adhesion and viability

Authors

Jhuliene Elen Muro Torrento, Tiago dos Santos Pereira de Sousa, Conrado Ramos Moreira Afonso, ..., Carlos Alberto Fonzar Pintão, Carlos Roberto Grandini, Diego Rafael Nespeque Correa

Correspondence

jhuliene.torrento@unesp.br (J.E.M.T.), diego.correa@unesp.br (D.R.N.C.)

In brief

Torrento et al. design low-cost, non-refractory TiZrNb-based high-entropy alloys that combine approximately 420 HV hardness with elastic modulus of 90–100 GPa. The alloys form protective passive films, resist tribocorrosion, and support early cell adhesion and viability, highlighting $Ti_{42}Zr_{22}Nb_{20}Fe_6Mn_6Al_4$ as a promising orthopedic biomaterial.

Muro Torrento et al., 2026, Cell Reports Physical Science 7, 103547
October 21, 2026 © 2026 The Authors. Published by Elsevier Inc.
https://doi.org/10.1016/j.xcrp.2026.103547

CellPress

Cell Reports
Physical Science

CellPress
OPEN ACCESS

Article

A low-cost and non-refractory high-entropy alloy for biomedical applications

Jhuliene Elen Muro Torrento,[1,7,*] Tiago dos Santos Pereira de Sousa,[1] Conrado Ramos Moreira Afonso,[2] Gerson Santos de Almeida,[3] Willian Fernando Zambuzzi,[3] Mariana Rocha Corrêa,[1] Marco Fosca,[4] Julietta V. Rau,[4,5] Silvia Spriano,[6] Graziano Ubertalli,[6] Giorgia Ghiara,[6] Carlos Alberto Fonzar Pintão,[1] Carlos Roberto Grandini,[1] and Diego Rafael Nespeque Correa[1,*]

[1]São Paulo State University (UNESP), School of Sciences, Campus Bauru, Laboratório de Anelasticidade e Biomateriais, 17033-360 Bauru, SP, Brazil
[2]Federal University of São Carlos (UFSCar), Department of Materials Engineering, 13565-905 São Carlos, SP, Brazil
[3]São Paulo State University (UNESP), Institute of Biosciences, Laboratório de Bioensaios e Dinâmica Celular, 18618-687 Botucatu, SP, Brazil
[4]Istituto di Struttura della Materia, Consiglio Nazionale delle Ricerche (ISM-CNR), Via Del Fosso del Cavaliere 100, 00133 Rome, Italy
[5]Department of Analytical, Physical and Colloid Chemistry, Institute of Pharmacy, Sechenov First Moscow State Medical University, Trubetskaya 8, Build. 2, 119048 Moscow, Russia
[6]DISAT Department, Institute of Materials Engineering and Physics, Politecnico di Torino, 10129 Torino, Italy
[7]Lead contact
*Correspondence: jhuliene.torrento@unesp.br (J.E.M.T.), diego.correa@unesp.br (D.R.N.C.)
https://doi.org/10.1016/j.xcrp.2026.103547

SUMMARY

The demand for metallic biomaterials that combine mechanical performance, corrosion resistance, biocompatibility, and affordability motivates the development of high-entropy alloys for orthopedic applications. Here, we report three TiZrNb-based alloys containing low-cost and non-refractory elements. The alloys predominantly exhibit body-centered cubic structures with secondary C14 Laves phase precipitation and dendritic microstructures characterized by chemical segregation. They combine high Vickers microhardness of approximately 420 HV with relatively low elastic modulus of 90–100 GPa. Stable passive films provide effective corrosion protection, while tribocorrosion tests reveal strong resistance to the combined action of wear and corrosion. Preliminary *in vitro* assays also demonstrate adequate cell adhesion and viability after 24 h. Among the investigated compositions, $Ti_{42}Zr_{22}Nb_{20}Fe_6Mn_6Al_4$ (atom %) provides the most favorable balance of economic, mechanical, physicochemical, and biological properties, highlighting its potential as a metallic biomaterial for future orthopedic applications.

INTRODUCTION

The increasing demand for durable, biocompatible implant materials has led to the widespread use of metallic biomaterials in orthopedical and dental applications. These materials are commonly used in load-bearing devices, such as plates, screws, and joint replacements. Currently, stainless steel (e.g., SS316L), cobalt-chromium (Co–Cr) alloys, and titanium (Ti) and its alloys dominate the market due to their favorable mechanical properties and corrosion resistance. Despite their widespread use, these conventional alloys still present limitations in long-term performance, biomechanical compatibility, and cost effectiveness. This scenario underscores the need to develop alternative metallic materials with optimized properties, particularly for bone fixation applications.[1,2]

High-entropy alloys (HEAs), a novel class of materials formed by combining five or more principal elements in near-equiatomic proportions, have emerged as promising candidates for advanced structural applications. The high configurational entropy of these systems favors the formation of solid solutions, resulting in enhanced mechanical strength, ductility, corrosion resistance, and wear resistance compared with conventional alloys. Although some HEAs have been proposed for biomedical applications, their potential for use in bone fixation devices remains underexplored compared with implants. This is particularly relevant given the stringent requirements for biocompatibility, mechanical compatibility, and cost effectiveness in biomedical applications. Moreover, many of the HEAs reported to date are based on expensive refractory elements with high melting points, limiting their practical applicability worldwide.[3–5]

The crystal structure of HEAs is highly sensitive to their elemental composition, atomic ratio difference, and processing conditions. Unlike conventional alloys, which often form multiple phases at equilibrium, many HEAs tend to form single-phase solid solutions. Depending on the solid solution, HEAs can exhibit face-centered cubic (FCC), body-centered cubic (BCC), or hexagonal close-packed (HCP) structures, as well as more complex phases such as Laves phases and intermetallic compounds.[6–9] Similarly, HEAs exhibit complex and variable microstructures that are influenced by the composition, processing techniques, and thermodynamic conditions. During solidification, many HEAs exhibit dendritic growth, forming tree-like

This is an open access article under the CC BY license (http://creativecommons.org/licenses/by/4.0/).

structures aligned with specific crystallographic directions. These dendritic microstructures play a crucial role in determining mechanical behavior, with finer dendrites generally contributing to improved strength and ductility.[10–13]

Chemical segregation is another critical issue in the microstructure of HEAs, commonly observed during solidification due to disparities in atomic size, electronegativity, and diffusion kinetics among the constituent elements. Such segregation often results in compositional inhomogeneities between the dendritic and interdendritic regions, which can significantly influence phase stability, mechanical properties, and corrosion behavior. A profound understanding of the effects of chemical segregation is essential for designing HEAs suitable for biomedical applications, where microstructural uniformity and long-term stability are crucial for reliable *in vivo* performance.[13–15]

From a mechanical standpoint, two key properties for evaluating metallic biomaterials are elastic modulus and hardness. An ideal bone implant material should exhibit an elastic modulus close to that of natural bone (~10–30 GPa) to minimize stress-shielding effects, while maintaining sufficient hardness to ensure mechanical integrity. Several HEAs, particularly those based on Ti, Zr (zirconium), Nb (niobium), and Ta (tantalum), have demonstrated promising mechanical properties that align with the requirements of biomedical applications. These characteristics position HEAs as attractive candidates for orthopedic devices that require both mechanical compatibility and durability.[15,16] Recent studies have further explored various HEA compositions for biomedical applications, focusing on biocompatible elements such as Ti, Zr, Nb, Ta, as well as hafnium (Hf) and molybdenum (Mo). Systems such as Ti–Zr–Nb–Ta, Ti–Zr–Hf–Nb, and Ti–Zr–Nb–Mo have demonstrated excellent corrosion resistance, cytocompatibility, and favorable mechanical properties, features essential for safe and effective implant performance.[15,17,18] The development of HEAs with biocompatible alloying elements is critical to ensuring not only the biological safety of implants but also their long-term integration and functionality within the human body.

In particular, TiZrNbTa systems have been widely investigated as benchmark compositions for biomedical applications due to their excellent combination of mechanical performance, corrosion resistance, and biocompatibility.[19–21] These alloys typically form single-phase BCC solid solutions after arc melting, with an elastic modulus of ~50–70 GPa, significantly lower than that of conventional Co–Cr alloys (~210–230 GPa) and closer to that of commercially pure Ti (~105 GPa).[19–21] Hardness values commonly range from ~220 to 324 HV, higher than those of commercially pure Ti (~120–200 HV) and lower than those of Co–Cr alloys (~450 HV).[20] Electrochemical studies in simulated body fluids have demonstrated low corrosion current densities (below 10 $\mu A/cm^2$) and stable passive behavior, comparable to or superior to those of Ti-based biomedical alloys.[20,21]

Nevertheless, the high content of refractory elements such as Nb and Ta, whose melting points exceed 2,673 and 3273 K, respectively, leads to elevated processing temperatures, increased energy consumption, and significantly higher raw material costs, which remain critical limitations to large-scale fabrication in the biomedical field.[22] Despite the promising characteristics of the system, the development of alternative multicomponent alloys containing minor amounts of refractory metals, with a predominant BCC crystal structure and suitable mechanical and biological properties, remains a challenge. In this context, Fe, Mn, and Al are attractive alloying candidates due to their low cost and melting temperatures and potential to improve the mechanical properties of Ti-based alloys.[23]

These considerations underscore the potential of HEAs to overcome the limitations of conventional metallic biomaterials, although their dependence on expensive refractory elements remains a major obstacle to large-scale biomedical applications. Here, from the $Ti_{50}Zr_{30}Nb_{10}Ta_{10}$ (at%) alloy composition, we design TiZrNb-based HEAs through the progressive substitution of Ta with the low-cost and non-refractory elements Fe, Mn, and Al, combined with adjustments in the Nb and Zr contents. The resulting alloys exhibit predominantly BCC structures with secondary C14 Laves phase precipitation and combine high hardness with relatively low elastic modulus. They also form stable passive films, comparable to Ti–6Al–4V, exhibit enhanced tribocorrosion resistance, and support early cell adhesion and viability. Among the investigated compositions, $Ti_{42}Zr_{22}Nb_{20}Fe_6Mn_6Al_4$ (atom %) provides the most favorable balance of economic, mechanical, physicochemical, and biological properties, highlighting its potential for future orthopedic applications.

RESULTS AND DISCUSSION

Role of the alloying elements in the microstructural features

The two-step melting process successfully produced ingots free of cracks or visible chemical segregation at the macro scale, indicating the absence of severe brittle behavior and adequate mixing of alloying elements. The experimental density values were closer to those calculated from the nominal values (Figure 1A), indicating a similar chemical composition. Furthermore, replacing refractory metals with light metals reduced the density from ~6.7 g/cm^3 (reference) to ~6.1 g/cm^3 for the HEA 2 sample. The slight discrepancy between the theoretical and experimental values may be attributed to chemical segregation caused by secondary-phase precipitation. The overall chemical composition acquired using energy-dispersive X-ray fluorescence spectroscopy (EDXRF) is shown in Figure 1B, where the nominal and experimental values of the alloying elements are compared. The average chemical proportion was taken from five measurements ($n = 5$) in millimetric regions. The results indicate good agreement with the selected stoichiometric values in some regions. However, some discrepancies, specifically for Mn, were observed and can be attributed to phase separation during ingot solidification, which may lead to chemical segregation. According to Balaji and Xavior,[24] large differences in melting points among alloying elements in multicomponent solid solutions, e.g., HEAs, can naturally lead to chemical segregation and phase separation. Despite this, the experimental values indicate that the samples have a representative chemical composition for the purposes of the current study.

Figure 2A shows the X-ray diffraction (XRD) patterns of the samples and the equilibrium phase proportion vs. temperature plot, calculated using ThermoCalc software (version 2025a) with the High Entropy Alloy database (TCHEA5, 2024).[25] The

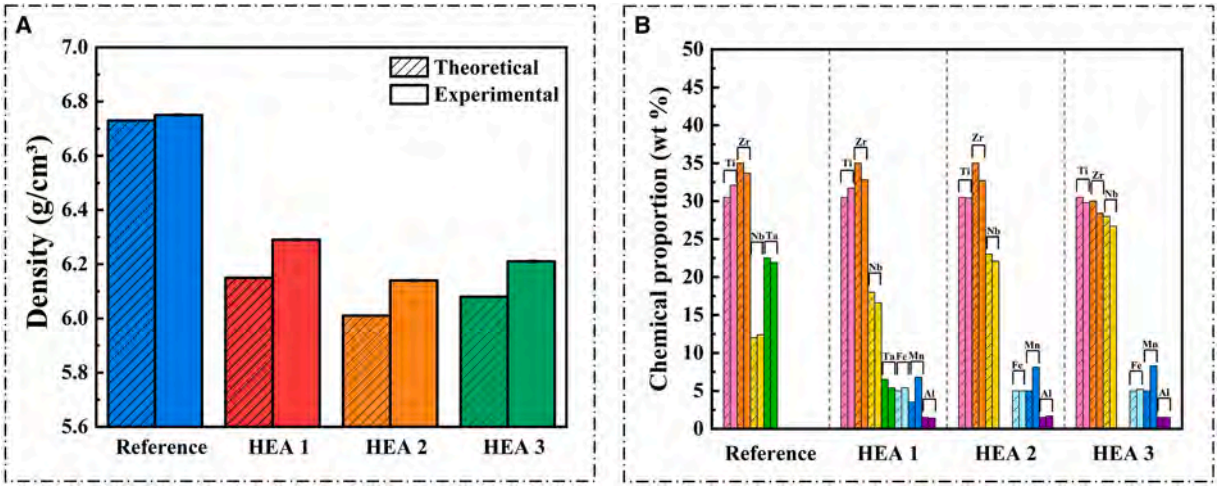


Figure 1. Density and chemical proportion

(A and B) Comparison of the as-cast ingots in terms of density (A) and experimental chemical composition (B). Error bars represent the standard deviation (n = 10).

reference sample exhibited peaks linked to a single BCC phase, consistent with previous reports on some TiZrNbTa compositions.[20,26] However, the HEA samples exhibited major peaks from a BCC phase coexisting with smooth peaks from a secondary HCP phase. A comparison with the corresponding equilibrium phases revealed that, around the heat-treatment temperature (1,273 K), the predominant phase for all samples was the BCC_B2 phase (green line, space group $Im\bar{3}m$). Given that a single BCC phase was detected in the reference sample, it is reasonable to infer that the applied cooling rate during heat treatment facilitates its retention at room temperature, thereby preventing the formation of secondary phases below 500 K. For the HEA samples, the fraction of the HCP phase could be related to the C14 Laves phase (red line, space group $P6_3mmc$). Thus, the equilibrium-phase proportion plots provide useful information on phase stability and phase formation tendencies in the investigated alloys. Although the calculations were performed under thermodynamic equilibrium conditions and, therefore, do not quantitatively represent the final microstructures obtained after arc melting and non-equilibrium cooling, they adequately predict the stability of the BCC phase and the tendency for the formation of the experimentally observed C14 phase. For comparison, Fang et al.[27] produced $Al_{0.8}Nb_{0.5}Ti_2V_2Zr_x$ ($0 < x < 0.9$) and observed that the Zr addition promoted the BCC → BCC + C14 Laves phase transition, with the BCC phase enriched in Ti and V and the C14 phase enriched in Zr and Al. The resulting dual-phase microstructure achieved a promising balance between mechanical strength and ductility.

In addition, a clear decrease in melting temperature was observed in the phase proportion plots upon alloying. The reference sample (1,940 K) has a melting temperature considerably higher than that of the other samples (1,627–1,672 K). Thus, minor replacements of refractory metals in solid solution significantly affect the melting point. Lastly, the presence of minor-phase fractions at temperatures below 1,200 K suggests that the microstructure could be fine-tuned through appropriate heat treatments, such as aging or solution treatment, yielding more manageable properties. For comparison, the success of Ti–6Al–4V in biomedical applications is strongly linked to its biphasic ($\alpha + \beta$) microstructure, which enables tailoring of mechanical properties by controlling the phase fraction and morphology. By adjusting thermomechanical processing and heat treatments, the balance between the α and β phases can be optimized, thereby tailoring strength, elastic modulus, and fatigue resistance to meet clinical requirements.[28]

The corresponding phase proportions and cell parameters obtained from the Rietveld refinement are shown in Figure 2B. The obtained merit parameters and details about the crystallographic data sheets are available in the supplemental files (Tables S1andS2; Figure S1). Overall, replacing the alloying elements promoted the coexistence of the BCC and C14 phases after furnace cooling, in contrast with the reference sample. Similarly, the cell parameter of the BCC phase exhibited a slight decrease, resulting from the distinct metallic atomic radii of the varied alloying elements: Ti (0.147 nm), Zr (0.160 nm), Nb (0.146 nm), Ta (0.146 nm), Fe (0.126 nm), Al (0.143 nm), and Mn (0.127 nm),[29] following Vegard's law. For the C14 phase, the cell parameters depict larger values compared with the conventional HCP structure found in metals and alloys, having a lattice-parameter ratio far from the theoretical value (1.633). This aspect indicates a distorted cell structure induced by the high-entropy solid solution, along with local plastic deformation driven by the major BCC phase in the crystal lattice.

Unlike HCP metals, where atoms occupy equivalent crystallographic sites in a relatively simple close-packed stacking sequence (ABAB), the C14 crystal structure is an intermetallic topologically close-packed (TCP) phase characterized by an AB_2 (e.g., $ZrMn_2$) stoichiometry and two non-equivalent atomic sites with distinct coordination environments. The atomic packing in the C14 phase involves complex polyhedral units, such as icosahedra and Frank-Kasper polyhedra, resulting in a larger unit cell and greater structural complexity than in HCP metals. As

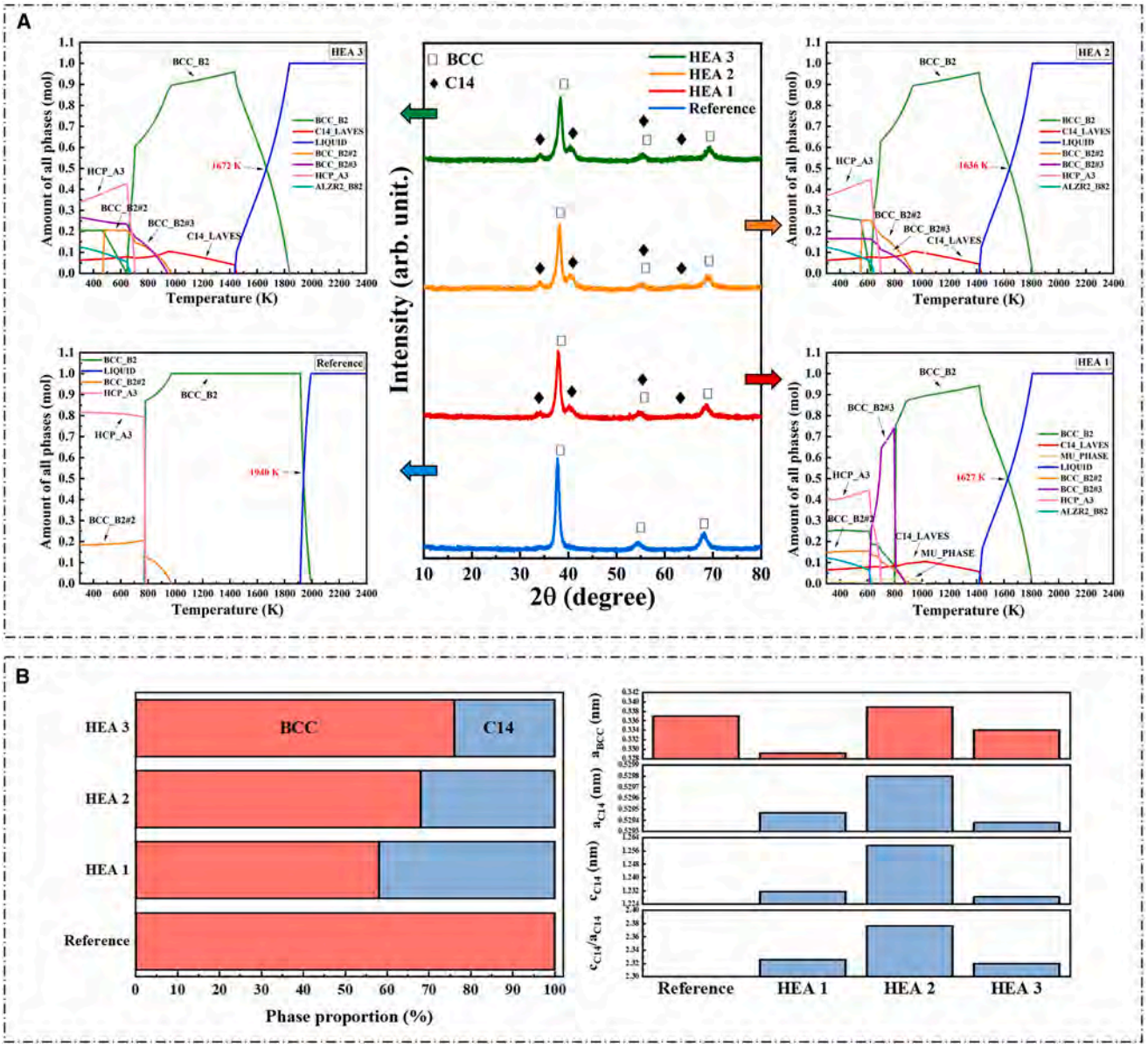


Figure 2. Sample characterization and comparison

(A) XRD profiles and the corresponding equilibrium phase-stability diagram.

(B) Phase proportions and lattice parameters obtained from Rietveld refinement.

reported in the literature, this structural arrangement promotes high hardness and limited plasticity due to strong atomic bonding and restricted slip systems, in contrast to the more deformable nature of conventional HCP metals. Therefore, the presence of the C14 phase in high-entropy systems is typically associated with increased strength and lattice distortion but may also contribute to brittleness depending on its volume fraction and distribution within the microstructure.[30]

Figure S2 shows the *in situ* EDXRD profiles of the samples acquired at different temperatures. Due to the low fraction and intensity of the diffracted peaks corresponding to the C14 phase, only the BCC phase peaks were indexed in all samples and used to evaluate the coefficients of thermal expansion (CTEs). In general, the BCC phase peaks shifted toward lower angles, indicating a gradual expansion of the cubic crystalline structure. In the diffractograms of the HEA 2 and HEA 3 samples, a peak from the C14 phase was also observed, which was not quantified but indicates its stability up to 773 K.

The evolution of the BCC cell parameter (a) with temperature is available in the supplemental file (Figure S3). The cell parameters were obtained from the interplanar spacing d, determined using Bragg's law and its relationship with the Miller indices (hkl), $d_{hkl} = \frac{a}{\sqrt{h^2+k^2+l^2}}$. All curves showed good agreement with a second-order polynomial fit, exhibiting the same

Table 1. Estimated CTE values of the samples

Sample	Correlation factor	CTE	A (K^{-1})	B (K^{-2})
Reference	0.96336	linear	2.3×10^{-5}	7.4×10^{-8}
		volume	6.5×10^{-5}	23.9×10^{-8}
HEA 1	0.89243	linear	1.4×10^{-5}	9.5×10^{-8}
		volume	3.4×10^{-5}	31.1×10^{-8}
HEA 2	0.98804	linear	4.9×10^{-5}	10.3×10^{-8}
		volume	14.1×10^{-5}	35.1×10^{-8}
HEA 3	0.99970	linear	4.0×10^{-5}	3.6×10^{-8}
		volume	11.8×10^{-5}	12.1×10^{-8}

temperature-dependent expansion behavior. These results were used to estimate the linear and the volumetric CTEs for the samples (Table 1). The correlation factor for each fitted curve remained ≥ 0.89, indicating good agreement with the experimental results.

The A coefficient represents the first-order CTE, while B corresponds to the second-order coefficient. It was observed that the alloying elements resulted in distinct variations in the A and B parameters across all evaluated crystalline aspects (cell parameter and volume). The A parameter exhibited a non-linear variation with the alloying elements and remained higher than that of metallic Ti ($\sim$0,86 $\times 10^{-5}$ K^{-1}).[31] On the other hand, the B parameter indicated that HEA 3 had the lowest value, suggesting greater thermal stability. From the volumetric CTE values, it is evident that the samples exhibited anisotropy, possibly due to alloying elements in solid solution and the presence of the C14 phase. Understanding the CTEs of the alloys is crucial for biomedical applications, as the CTE plays an important role in adhesion of an implant's surface with ceramic coatings used in dental[32] and orthopedic[33] surgeries.

Microstructural features of the samples, as observed by optical microscopy (OM) and scanning electron microscopy (SEM), are shown in Figure 3A. In the reference sample, grain boundaries associated with the BCC phase can be identified. In contrast, the other samples depict a clear dendritic formation, typical of HEAs. The dendritic structures correspond to two distinct phases, corroborating the XRD results and consistent with previous studies reporting changes in the phase composition of HEAs.[27,34–36] In the SEM images, grain sizes up to 100 μm and dendrites with an average length of 50–100 μm and a width of 10 μm were observed, with no clear variation between the samples. Furthermore, small precipitates (>5 μm) were found throughout the dendrites, with varying numbers and sizes depending on the alloying elements. Additionally, the backscattered (BSD) images showed fine Z-contrast between the dendritic phases, with some dendrites having a distinct gray tone, indicating enrichment with light elements. This contrast reveals localized chemical segregation between phases, as expected from the phase proportion diagram shown in Figure 2A and the complex cooling mechanisms of multicomponent solid solutions.[14]

The chemical mapping of the HEA samples obtained by energy-dispersive X-ray spectroscopy (EDS) is shown in Figure 3B, where all alloying elements were tracked throughout the dendritic structures. The images show clear chemical segregation within the dendrites, confirming the presence of two major phases in the microstructure. One phase is enriched mostly in Ti and Nb, while the second is enriched in Zr, Fe, Al, and Mn, with Ta distributed in both phases in the HEA 1 sample. Overall, the TiNb-rich dendrite is identified as the BCC phase, while the ZrFeAlMn-rich dendrite is identified as the C14 phase. As already reported by Mishra et al.,[30] El Aalami et al.,[37] and Stein and Leineweber,[38] the C14 phase is formed in the typical stoichiometry AB_2, where A is occupied by the large-sized element (Zr) and B by the small ones (e.g., Fe, Al, and Mn), being found in diverse multicomponent solid solutions (e.g., Zr–Fe–Mn, Zr–Fe–Al, and Ti–Zr–Fe–Mn–Cr).

To further investigate the nanoscale phase composition of the most promising designed sample (HEA 3), a focused-ion-beam (FIB)-prepared lamella was examined using transmission electron microscopy (TEM), and the results are shown in Figures 4A–4H. Figures 4A and 4B depict an overview of the FIBed lamella acquired at low magnification in bright-field (BF) and high-angle annular dark-field (HAADF) modes, respectively. Then, the region enclosed by the green dashed square was selected for a zoomed view based on Z-contrast, which delineates the boundary between two distinct phases. The boundary region (Figures 4C and 4D) exhibited a smooth contour between the BCC and C14 phases, indicating stable alignment of crystallographic planes, typical of a semi-coherent interface. The selected-area electron diffraction (SAED) patterns collected for each phase (Figures 8E and 8F) showed distinct spot distributions (Figures 4G and 4H), supporting the presence of the BCC and C14 phases. The SAED marked in red matches with the $[0\bar{1}0]_{BCC}$ zone axis, while the blue one matches with the $[001]_{C14}$ zone axis.

The crystallographic features observed at the interface are consistent with the structural correspondence described by Hirata and Koyama[39] for the Fe–Ti alloy system. In their study, a specific crystallographic relationship between the BCC and C14 Laves phase ($MgZn_2$-type, hexagonal, $P6_3/mmc$) was identified, demonstrating that atomic-plane matching and geometric compatibility can occur between these structures.

The high-resolution image of the interface between the phases obtained by high-resolution TEM (HRTEM), along with the corresponding fast Fourier transform (FFT) images, is shown in Figures 9I–9M. The planar distances (inset of Figure 4I) indicated a large value for the C14 phase compared with the BCC, in agreement with the differences in the crystal lattice parameters calculated with the Rietveld refinements (Figure 2B). The FFT images collected in the distinct phases show spot distributions similar to those predicted in SAED profiles, matching with the $[0\,0\,0\,1]_{C14}$ and $[\,1\,1\,0]_{BCC}$ zone axis at the interface. Once again, the orientation relationship observed between the BCC and C14 phases at the interface is consistent with the crystallographic correspondence reported by Hirata and Koyama.[39] In their work, specific parallelisms between close-packed planes and directions of the BCC structure and the basal and prismatic planes of the C14 phase were identified, demonstrating geometric lattice matching between the two structures. This correspondence arises from similarities in atomic stacking sequences and interplanar spacings, which allow partial accommodation of

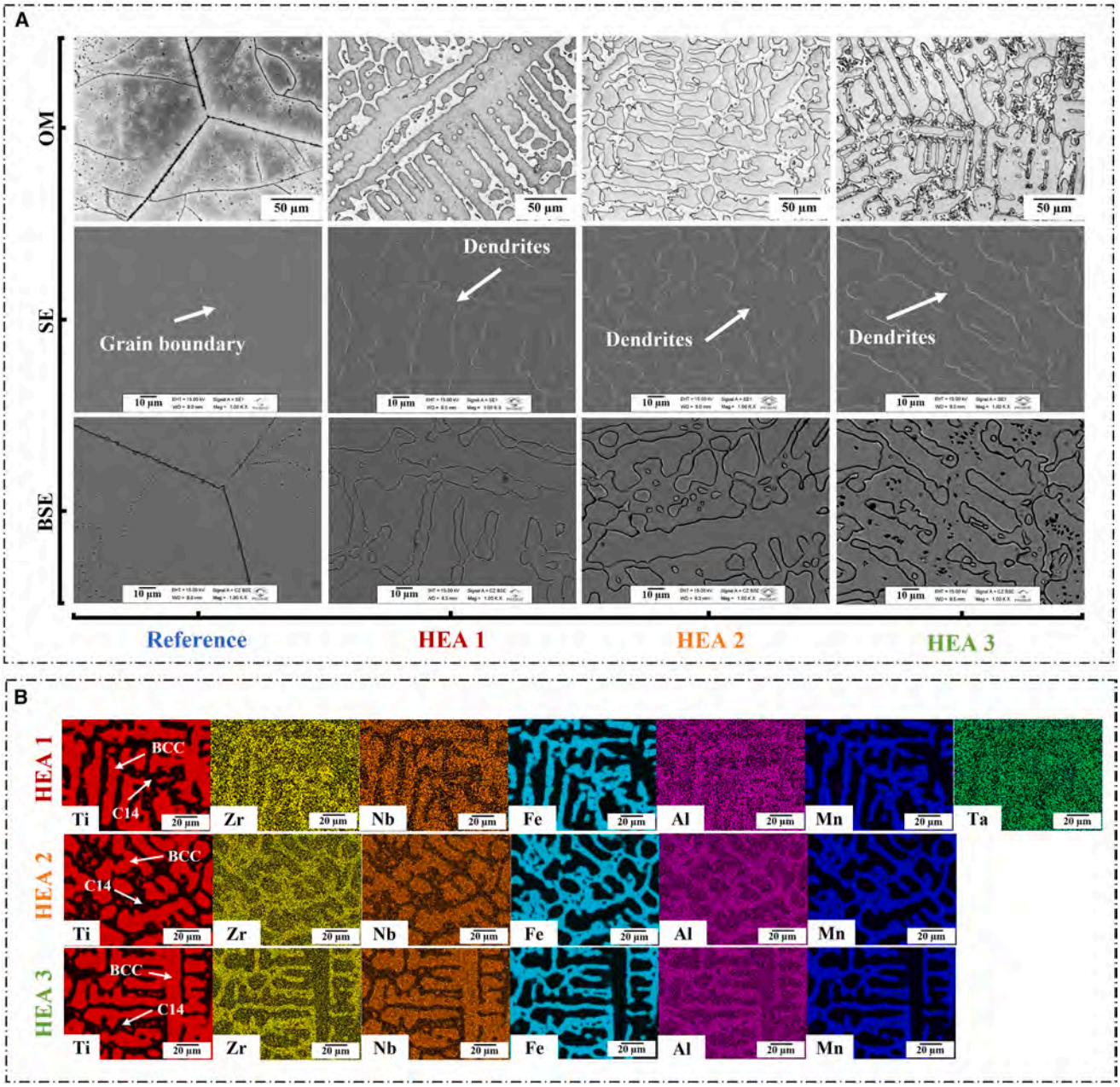


Figure 3. Microstructure and chemical mapping

(A) Microstructural details of the samples (scale bars: 10 μm).

(B) EDS chemical mapping of the samples (scale bars: 20 μm).

lattice mismatch through elastic strain, rather than through the formation of misfit dislocations. The alignment of the $[0\ 0\ 0\ 1]_{C14}$ and $[1\ 1\ 0]_{BCC}$ zone axes, observed in the present study, suggests a comparable crystallographic compatibility, supporting the existence of a low-energy interface. Therefore, the combined HRTEM and FFT analyses reinforce the classification of the BCC/C14 boundary as possibly semi-coherent, with lattice continuity across the interface contributing to structural stability in the multiphase HEA system. Further studies of the crystallographic features at the phase interface can provide valuable insights into the solidification and phase stabilization of solid solutions.

The FIBed lamella was also submitted to semi-quantitative chemical analysis at the interface, as shown in Figure 5. The chemical mapping results (Figure 5A) are consistent with the previous EDS-SEM analysis (Figure 3B), where the preferential chemical segregation of the Ti and Nb atoms in the BCC phase and Zr, Fe, Mn, and Al in the C14 phase could be clearly seen.

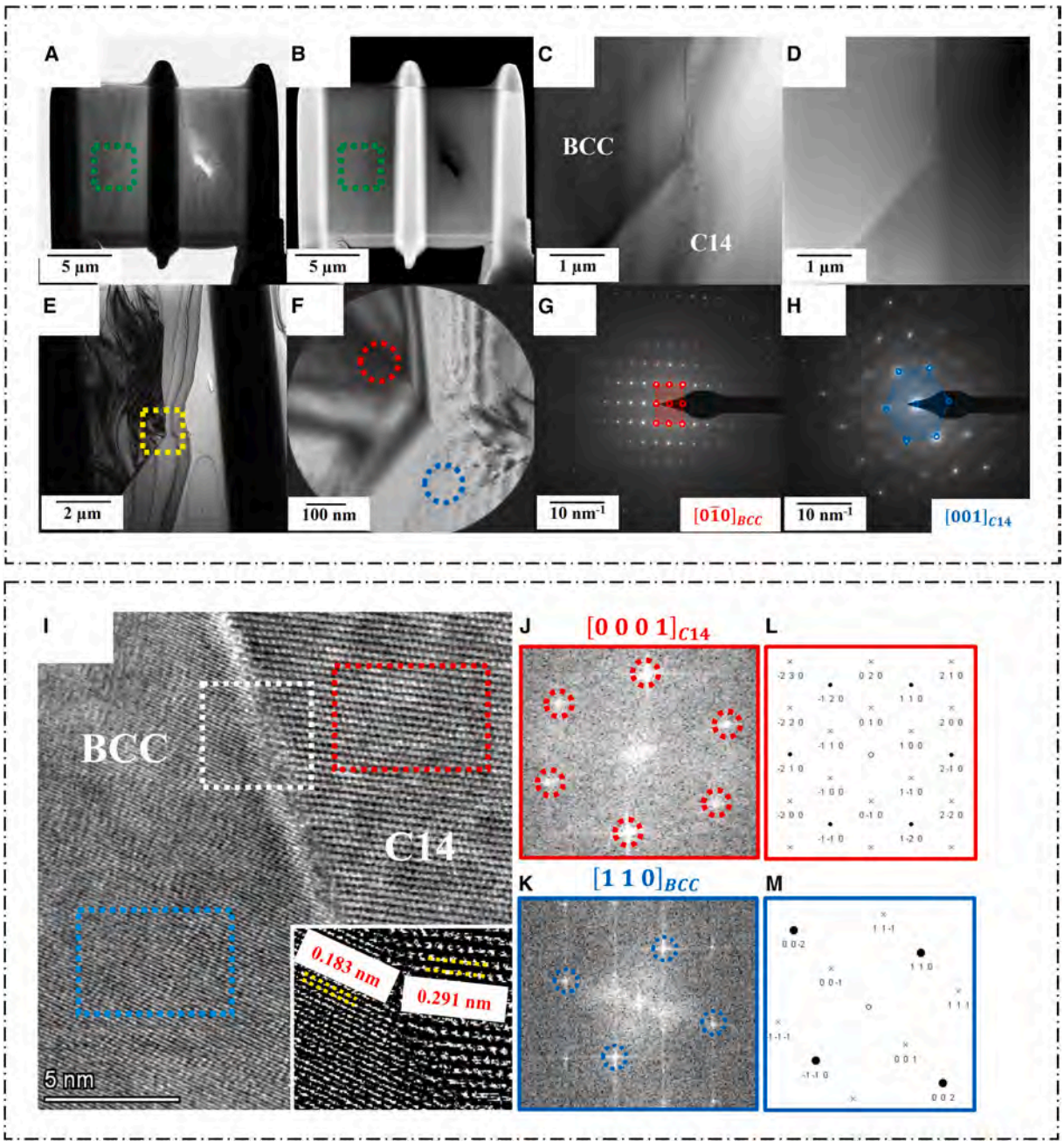


Figure 4. TEM imaging of the HEA 3 sample

(A and B) BF-STEM (A) and HAADF-STEM (B) images of the FIBed lamella (scale bars: 5 μm).

(C and D) BF-STEM (C) and HAADF-STEM (D) images of the zoomed view indicated by the green dashed square in (A) and (B) (scale bars: 1 μm).

(E and F) DF-TEM image indicating the interface between the phases (scale bar: 2 μm) (E) and zoomed region (F) of the yellow dashed square (scale bars: 100 nm).

(G and H) The corresponding SAED patterns taken in the BCC (red) (G) and C14 (blue) phases (H) (scale bars: 10 nm^{-1}).

(I) HRTEM image at the interface between the BCC and C14 phases: overall image (I) (scale bars: 5 nm) and the planar distance as an inset of the white dashed square.

(J–M) FFT profile of the C14 (J) and BCC (K) phases, and corresponding spot distribution of the matched zoned axis of the C14 (L) and BCC (M) phases.

Furthermore, the line scan (Figure 5B) showed a smooth variation in the chemical composition across phases, supporting the presence of a semi-coherent interface. Figure 5C shows the chemical proportions of the alloying elements at the interface, which remain close to the nominal values, indicating that the overall chemical composition is respected at the sub-micrometric scale.

A similar chemical partitioning behavior between the BCC and C14 phases was reported by Zhao et al.[40] in AlNbTiVZr

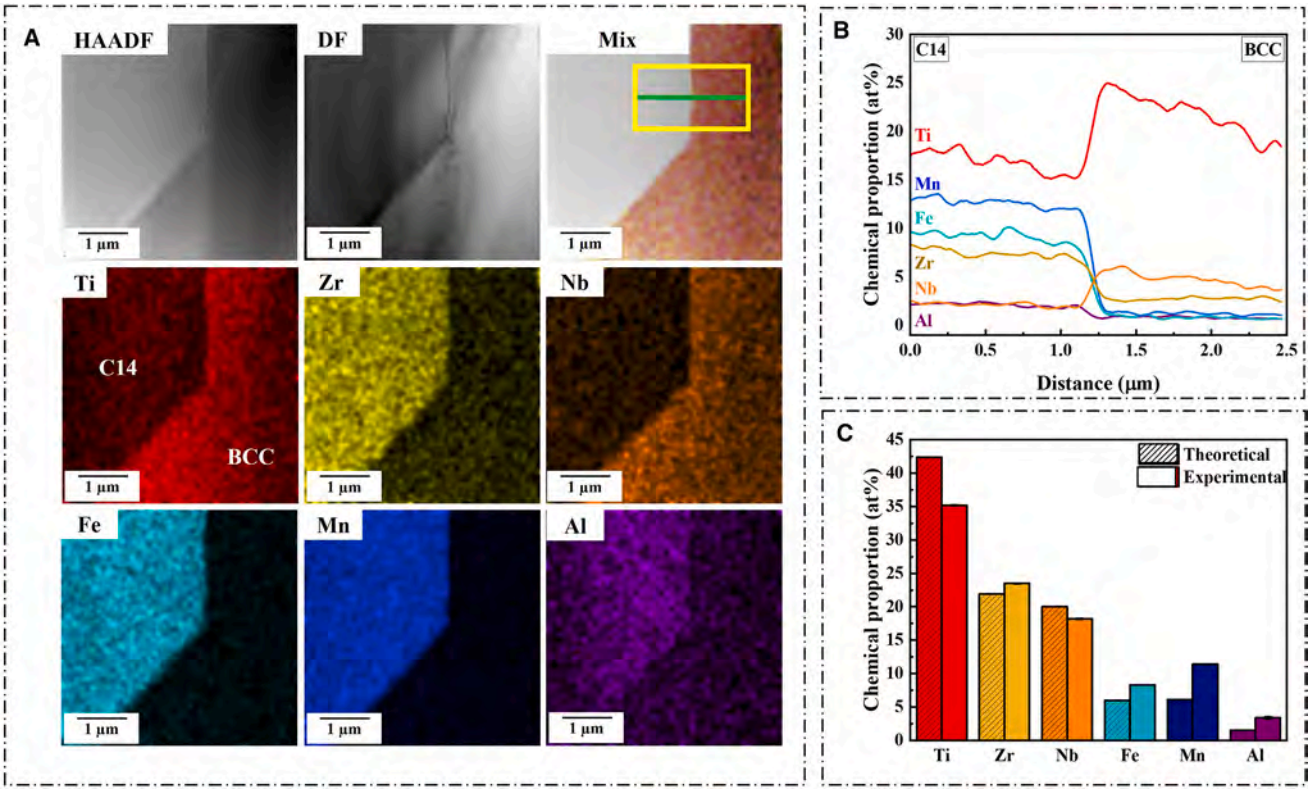


Figure 5. Semi-quantitative results of the FIBed sample

(A) BF-STEM and HAADF-STEM images and the corresponding elemental EDS mapping at the phase interface (scale bars: 1 μm).

(B and C) Chemical profile acquired in the line scan mode of the green line (B), and overall chemical proportion acquired in the yellow square (C). Error bars represent the standard deviation (n = 3).

lightweight refractory HEAs. In their study, a detailed compositional analysis revealed preferential segregation of refractory elements into the BCC matrix and enrichment of specific elements within the C14 phase, generating compositional gradients at the interface. This controlled phase separation was directly correlated with mechanical performance, with the transformation of the C14 phase morphology from a continuous network to a dispersed distribution leading to simultaneous increases in yield strength and ductility.

Relationship between composition, microstructure, and selected properties

The selected mechanical properties of the HEA and reference samples are shown in Figure 6. The elastic modulus values of the HEA samples (Figure 6A) remained higher than that of the reference sample (~48 GPa), which aligns well with the value reported in the literature.[26] Furthermore, all values remained below those of commercially pure Ti grade 2 (CP-Ti, ~100 GPa) and the Ti–6Al–4V alloy (Ti-64, ~110 GPa). The increase in the elastic modulus can be attributed to the combined effect of chemical bonding and phase precipitation. Firstly, the addition of alloying elements decreases the BCC cell parameter for HEA 1 and HEA 3, as shown in Figure 2B, thereby increasing chemical bonding between atoms and altering the energy required for atomic displacement.[15,41,42] Regarding the phase precipitation effect, the presence of the C14 phase tends to increase the elastic modulus because the crystal lattice has different slip planes from those in the BCC phase, as typically observed in Ti-based alloys.[43]

Figure 6B presents the Vickers microhardness values for the HEA samples compared with the reference. The HEA samples exhibited values around 420 HV, higher than that of the reference sample (356 HV) and above those of CP-Ti (145 HV) and Ti-64 (349 HV). Similarly, this increase can be attributed to solid-solution strengthening and phase-precipitation hardening effects. The chemical segregation between dendrites, as shown in Figures 3B and 5A, can form solid solutions with varying amounts of hardener elements, resulting in a distorted crystal structure that hinders atomic movement during plastic deformation.[44] This inference is also supported by the distinct values taken in each dendrite, as shown in the indentation image of Figure 6B. Furthermore, the coexistence of a dual phase in the microstructure can mitigate dislocation movement across the phase interface during plastic deformation, thereby increasing hardness.[28]

The corrosion test results for the HEA and reference samples are shown in Figure 7 and Tables 2, 3, and 4. Figure 7A presents the anodic polarization curves of the samples, which are used to characterize their passivation behavior and quantitatively assess their corrosion resistance relative to the Ti-64 alloy. A qualitative

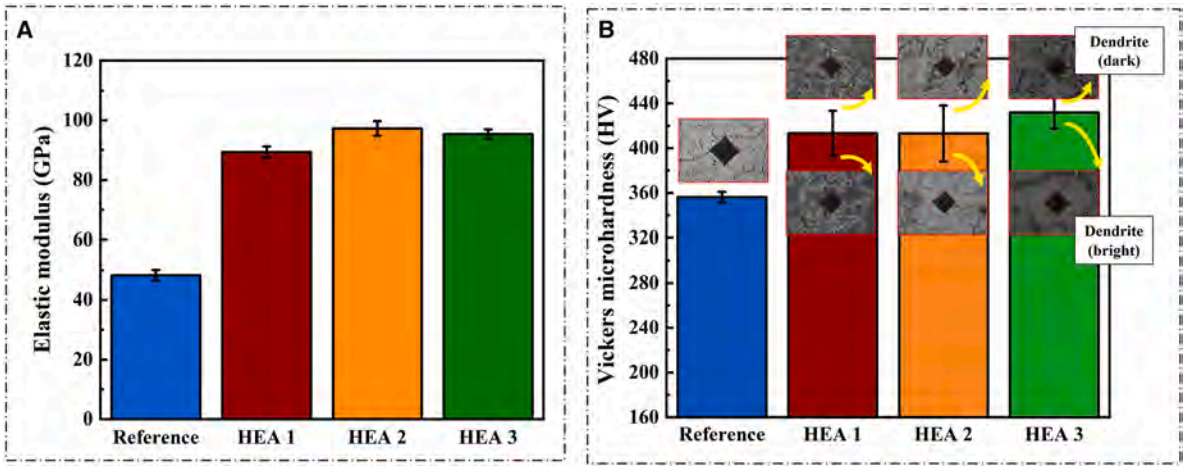


Figure 6. Selected mechanical properties of the sample

(A) Elastic modulus.

(B) Vickers microhardness.

Error bars represent the standard deviation (n = 10).

analysis of the polarization curves enabled identification of key electrochemical parameters, including the corrosion potential (E_{corr}), passive current density, and the extent and stability of the passive region. These parameters enabled a direct comparison of the protective performance of the passive films formed on each alloy. Table 2 summarizes the corresponding values for each tested material. The results indicate that alloy HEA 2 exhibits the lowest E_{corr}, with an E_{corr} of −0.417 ± 0.004 V vs. Ag/AgCl (sat. KCl), suggesting a comparatively higher thermodynamic tendency toward corrosion. This is followed by HEA 1 (E_{corr} = −0.380 ± 0.007 V vs. Ag/AgCl, sat. KCl) and the reference alloy (E_{corr} = −0.349 ± 0.001 V vs. Ag/AgCl, sat. KCl). HEA 3 displays the most positive E_{corr} among the investigated HEAs, with an E_{corr} of −0.277 ± 0.003 V vs. Ag/AgCl (sat. KCl), indicating the most noble electrochemical behavior within this group. The Ti-64 alloy exhibits an intermediate E_{corr} of −0.356 ± 0.017 V vs. Ag/AgCl (sat. KCl), falling between those of HEA 1 and the reference sample. The corresponding corrosion current density of the studied samples remains at the same level as the Ti-64 alloy, except for HEA 3, which exhibits a beneficial lower value. Consistent with these trends, the pitting potential (E_{pit}) is the lowest for HEA 2 (0.669 ± 0.007 V vs. Ag/AgCl, sat. KCl), indicating the earliest onset of localized passive film breakdown. Higher E_{pit} values are observed for HEA 1 (0.741 ± 0.006 V vs. Ag/AgCl, sat. KCl) and HEA 3 (0.844 ± 0.008 V vs. Ag/AgCl, sat. KCl), reflecting a progressively improved resistance to pitting corrosion. Notably, the reference sample exhibits an E_{pit} very close to that of the Ti-64 alloy (0.924 ± 0.009 V vs. Ag/AgCl, sat. KCl and 0.976 ± 0.013 V vs. Ag/AgCl, sat. KCl, respectively), highlighting its excellent resistance to localized corrosion over an extended potential range.

However, when considering the passive current density (Figure 7B), the reference sample exhibits the least favorable behavior, with a value of approximately 1.30 $\mu A \cdot cm^{-2}$, which is up to 2 times higher than those of the other alloys. In contrast, HEA 1, HEA 2, and HEA 3 display comparable passive current densities, averaging 0.5–0.7 $\mu A \cdot cm^{-2}$, indicative of more compact and protective passive films, comparable to that formed on the Ti-64 alloy. Calculations of the passive potential interval further confirm that all samples possess passivity over a wide potential window, underscoring the stability and protective effectiveness of the passive films formed on their surfaces. These results can be explained by pitting corrosion of the C14 phase in the HEA samples (with the greatest pitting on the secondary phase of HEA 2 and the least on HEA 3), driven by chloride ions. In the absence of secondary phases, the reference alloy and Ti-64 have similar, higher resistance to localized corrosion. On the contrary, the HEA samples show a similar increase in the passive layer's protective ability to that of Ti-64 and the reference sample (the lowest). The results obtained are consistent with those reported in the literature. Typical E_{corr} values in PBS for metal alloys used in the biomedical field are in the range of −0.1 V (Co–Cr alloys),[45] −0.2 V (SS316L),[46] −0.5 V (Ti-64).[47] Ti-64 and Co–Cr alloys typically do not exhibit pitting corrosion, but an E_{pitt} of +0.56 V has been reported for SS316L.

Figure 7C reports some micrographs of the samples observed after the anodic polarization curves, while Table 3 reports the corresponding semi-quantitative EDS analysis. Pitting corrosion of the interdendritic C14 phase was clearly observed in the HEA samples, whereas general corrosion was found to occur in the reference sample and the Ti-64 alloy. The corroded areas were qualitatively less extensive on HEA 3, while features with a filamentous appearance were well evident on HEA 2. The EDS analysis of the samples after polarization is close to expectations, given the theoretical and experimental compositions of the alloys. The reported values are derived from both the oxide layer and the metal alloys due to the electron probe's penetration depth in EDS analysis. Ta was largely detected at the surface of the reference sample, likely due to its presence in the surface oxide layer. Further chemical analysis by X-ray photoelectron spectroscopy (XPS) and long-term corrosion tests can provide additional insights into the surface chemistry and corrosion mechanisms, respectively.

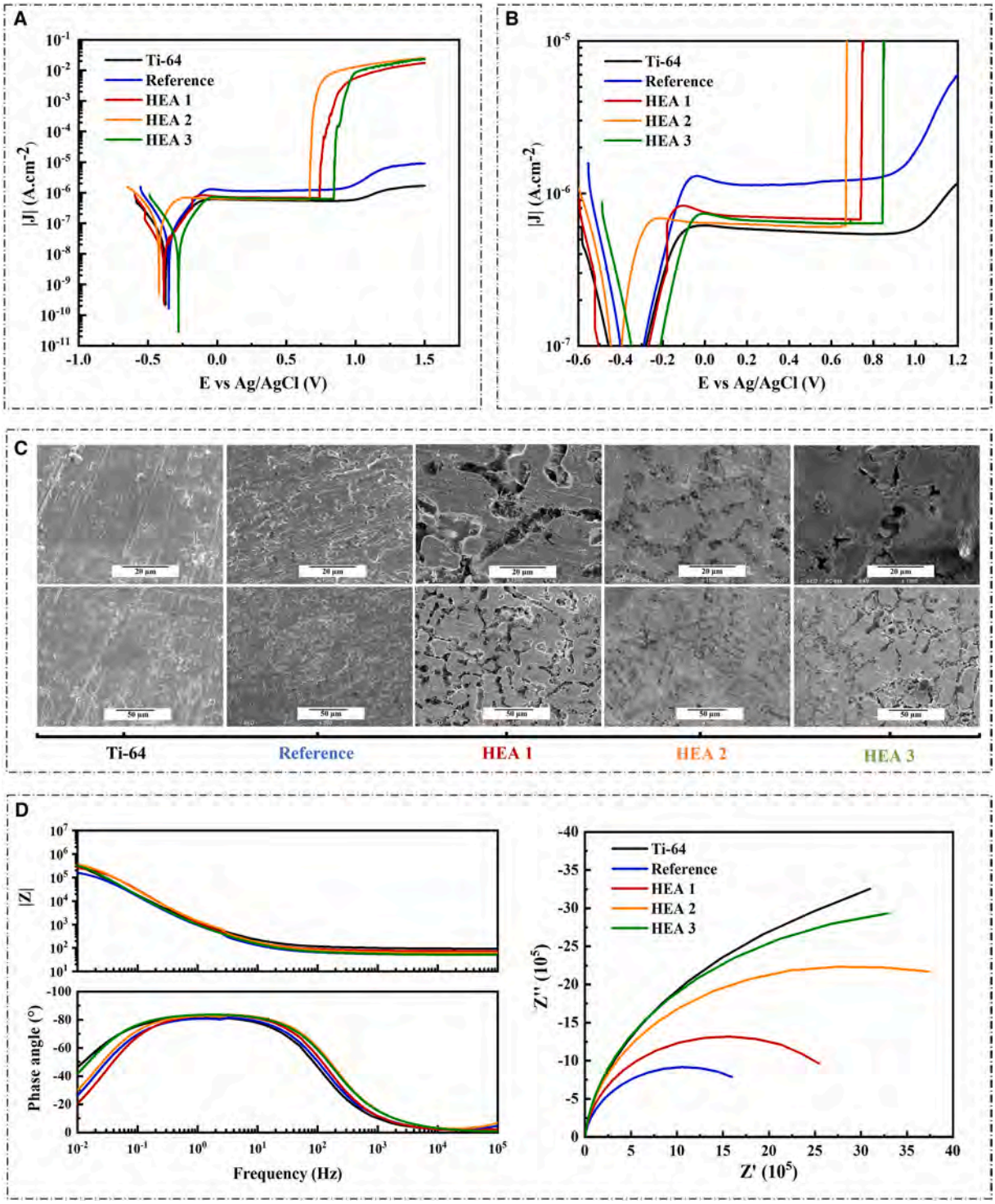


Figure 7. Corrosion tests

(A and B) Anodic polarization curves in aerated PBS solution (A), and enlargement of anodic polarization curves in aerated PBS solution (B).

(C) SEM images of the samples after anodic polarization (scale bars: 20 and 50 μm).

(D) EIS Bode and Nyquist plots of the samples in PBS solution after stabilization of the OCP.

Table 2. Electrochemical parameters obtained from the anodic polarization curves

Sample	E_{corr} (V)	E_{pit} (V)	Passive E interval (V)	J_{pass} ($\mu A \cdot cm^{-2}$)
Ti-64	−0.356 ± 0.017	0.976 ± 0.013	1.036 ± 0.013	0.579 ± 0.039
Reference	−0.349 ± 0.010	0.924 ± 0.009	0.992 ± 0.010	1.290 ± 0.154
HEA 1	−0.380 ± 0.007	0.741 ± 0.006	0.858 ± 0.007	0.799 ± 0.127
HEA 2	−0.417 ± 0.004	0.669 ± 0.007	0.924 ± 0.010	0.695 ± 0.094
HEA 3	−0.277 ± 0.003	0.844 ± 0.008	0.879 ± 0.008	0.754 ± 0.121

Electrochemical impedance spectroscopy (EIS) measurements were performed on each sample after the open-circuit potential (OCP) stabilized for 2 h. The results are presented in both Bode and Nyquist representations (Figure 7D). The Bode phase plots (phase angle versus frequency) reveal distinct time constants ($\tau = RC$), which are associated with the dominant electrochemical processes occurring at the alloy-solution interface. For all samples, a single predominant time constant was observed across the explored frequency range, indicating that the interfacial response is governed by a single process, likely related to the electrochemical behavior of the passive film formed on the metallic surface, possibly composed of TiO_2 doped with different metal cations. From the Nyquist plots (Z'' vs. Z'), it is possible to assess the magnitude of the interfacial process and distinguish its resistive (R) and capacitive (C) contributions. In all cases, the impedance response was characterized by a single capacitive loop, consistent with a single dominant electrochemical process controlling the system response. Qualitatively, the Ti-64 alloy exhibited the highest overall impedance, followed by HEA 3, HEA 2, HEA 1, and the reference sample, in decreasing order. The reference sample showed the smallest semi-circle, suggesting the lowest interfacial resistance and, consequently, a comparatively weaker barrier to charge transfer.

An electrical equivalent circuit (EEC) was employed to model the electrochemical behavior of each sample. The presence of a single time constant in the Nyquist plots allowed the curves to be represented by a single R//CPE (constant phase element) branch, capturing the dominant interfacial process. The single time constant specifically represents the properties of the oxide layer at the interface with the solution. The use of a CPE, instead of pure capacitance (C), accounts for the dispersive behavior of the passive oxide film, reflecting surface heterogeneities and non-ideal capacitive behavior. In addition, a solution resistance (R_s) was included in the circuit to account for the ohmic resistance of the electrolyte between the working electrode (WE) and reference electrode (RE) (Figure S4).

Fitting results are summarized in Table 4, along with a detailed attribution of their corresponding electrochemical parameters. The data indicate that HEA 3 exhibits the most favorable resistive behavior of the passive film (597 $k\Omega \cdot cm^2$), with values approximately two to three times higher than those measured for HEA 1 (292 $k\Omega \cdot cm^2$) and the reference sample (206 $k\Omega \cdot cm^2$). Overall, the performance of HEA 3 is comparable to that of the reference Ti-64 (660 $k\Omega \cdot cm^2$), with similar film resistance values and a similarly robust and stable passive film at the alloy-solution interface. HEA 2 exhibits intermediate behavior, with resistance values not too far from those of HEA 3 (488 $k\Omega \cdot cm^2$), suggesting a moderately protective passive layer. A computational analysis was also performed using Brug's equation to determine the apparent interfacial capacitance, which, in this context, represents the effective capacitance of the passive film alone, providing further insight into the dielectric properties and integrity of the oxide layer, $C_{eff}\left(C_{ox} = Q^{1/n} \times R_{ox}^{(1-n)/n}\right)$, where Q and n represent the CPE value and coefficient, respectively, while R_{ox} corresponds to the oxide resistance. Results from this analysis show that the reference sample exhibits the highest capacitance, which, from a physical perspective, may indicate a thinner yet homogeneous oxide layer. Comparable capacitance values were observed for the HEA samples and the Ti64 alloy. These minor differences could arise not only from variations in oxide thickness but also from subtle changes in the oxide composition, reflecting the influence of the specific alloying elements present in each material. Considering the stability of oxide formation from the alloying elements and their chemical proportions in the bulk, it is expected that protection against corrosion arises primarily from Ti-, Zr-, Nb-, and Ta-based oxides, at the expense of the Al-, Fe-, and Mn-based ones. Further XPS analysis can reveal more aspects about the chemical composition of the passive layer.

The results of the tribocorrosion tests on the HEA and reference samples are shown in Figures 8A–8D, and the corresponding wear-track topographies are presented in Figure 8E. The coefficient of friction (COF) values of the HEA samples remained below those of the reference samples (Figure 8A), suggesting a positive lubricating effect of the surface that mitigates the wear mechanism. Regarding the OCP values (Figure 8B), the results are again positive compared with the reference sample. Before

Table 3. EDS analysis of the samples after anodic polarization

Sample	O	Al	Ti	V	Mn	Fe	Zr	Nb	Ta
Ti64	–	5.78	89.97	4.25	–	–	–	–	–
Reference	8.76	–	31.69	–	–	–	27.36	–	32.19
HEA 1	12.42	1.51	23.41	–	9.18	7.83	29.45	10.84	5.36
HEA 2	22.98	0.98	25.39	–	8.69	6.09	22.24	13.64	–
HEA 3	13.94	1.37	26.79	–	6.50	4.16	23.78	23.47	–

Table 4. Fitting results using the EECs all considered alloys

Sample	R_s ($\Omega \cdot cm^2$)	R_{ox} ($k\Omega \cdot cm^2$)	CPE_{ox} Q (Ω^{-1} $cm^{-2} \cdot s^n$)	CPE_{ox}-n	$C_{eff\ ox}$ ($F \cdot cm^{-2}$)
Ti64	100 ± 0.4	660 ± 8	$2.09 \cdot 10^{-5} \pm 0.001 \cdot 10^{-5}$	0.92 ± 0.01	$2.60 \cdot 10^{-5} \pm 0.007 \cdot 10^{-5}$
Reference	55 ± 0.2	206 ± 2	$3.18 \cdot 10^{-5} \pm 0.01 \cdot 10^{-5}$	0.92 ± 0.01	$3.71 \cdot 10^{-5} \pm 0.01 \cdot 10^{-5}$
HEA 1	78 ± 0.3	292 ± 1	$1.81 \cdot 10^{-5} \pm 0.004 \cdot 10^{-5}$	0.94 ± 0.01	$1.99 \cdot 10^{-5} \pm 0.004 \cdot 10^{-5}$
HEA 2	65 ± 0.4	488 ± 5	$1.60 \cdot 10^{-5} \pm 0.006 \cdot 10^{-5}$	0.94 ± 0.01	$1.82 \cdot 10^{-5} \pm 0.007 \cdot 10^{-5}$
HEA 3	56 ± 0.3	597 ± 8	$2.04 \cdot 10^{-5} \pm 0.007 \cdot 10^{-5}$	0.94 ± 0.01	$2.40 \cdot 10^{-5} \pm 0.008 \cdot 10^{-5}$

sliding, the OCP value for the reference sample was the lowest (−0.32 V), indicating a less protective oxide layer than that of the HEA samples. During sliding, all samples exhibited typical OCP decay and fluctuations, resulting from the alumina ball removing the oxide layer and thereby exposing the metallic surface to the solution. As a result, an increase in the current density passing through the sample was also noticed (see Figure S5). In addition, the reference sample showed a slight linear trend over time, suggesting the presence of a foreign protective layer, such as a tribolayer formed by adhered debris. After sliding removal, the HEA samples also performed better than the reference sample, particularly HEA 3 (with the highest Nb content), which exhibited the best repassivation behavior. Lastly, the power vs. time plot (Figure 8C), which allows estimation of the total energy transferred to the sample, indicated that the average value for the HEA 3 sample was the lowest, resulting in minimal surface wear damage. The corresponding topography of the wear track (Figure 8E) shows grooves, a common feature of abrasive wear. However, some black regions (BSD image) were observed in the reference sample, suggesting the presence of adhered particles that form tribolayers and supporting the OCP fluctuations observed during sliding. In agreement with the previous results, the wear loss volume (Figure 8D), obtained by Z-view of the wear tracks (see Figure S6) revealed a significant reduction, with values lower than half of those observed for the reference sample across all HEA samples, which can be attributed to their improved mechanical stability and the formation of a more protective tribolayer during sliding. Further dry wear and corrosion tests under the same conditions can give insights into the synergism between these degradation mechanisms and the role of the chemical composition.

Figure 9A shows the wettability results for each sample, presented as contact angles measured in distilled water and glycerol, along with the corresponding surface energies. The contact angle varied significantly across the samples, indicating that the chemical composition of the passive layer is distinct and influences the surface hydrophilicity. It is important to note that all samples possess a slightly hydrophilic character (contact angle < 90°), which may facilitate cell adhesion and proliferation.[48,49] The use of both distilled water and glycerol enables the separation of the polar and dispersive components of surface energy, which are critical in biomaterials, as surface wettability governs protein adsorption and subsequent cellular responses. Notably, HEA 2 exhibits an anomalous value relative to the other alloys, suggesting distinct behavior. The respective surface energies were calculated and are presented in Figure 9B. The total surface energy was almost entirely dispersive, similar for all samples, indicating minor variations in surface characteristics among the compositions, except for HEA 2, which exhibited a slightly lower value. This behavior follows the slight differences observed in the wettability. According to previous studies, surfaces exhibiting moderate hydrophilicity and medium-to-high surface energy are considered favorable for biomaterial applications, as they promote balanced protein adsorption and subsequent cell adhesion.[50] In this context, all alloys fall within or close to this biologically relevant range.

The preliminary *in vitro* biological responses of the samples are shown in Figures 9C and 9D. Cell adhesion, evaluated by the crystal violet (CV) assay after 24 h of culture in conditioned media, revealed that all HEA samples and the reference alloy present levels similar to the control group ($p > 0.05$), indicating no adverse effects on initial cell attachment. Regarding cell viability, assessed using the MTT ((3-(4,5-dimethylthiazol-2-yl)-2,5-diphenyltetrazolium bromide) assay, all samples exhibited values above the 70% threshold established by ISO 10993-5[51] for non-cytotoxicity. Notably, the reference alloy induced a statistically significant increase in metabolic activity compared with the control ($^*p < 0.05$), while all HEA samples (HEA 1, HEA 2, and HEA 3) promoted an even more pronounced increase, with $^{****}p < 0.0001$ relative to the control. These findings demonstrate that the developed HEAs are not only cytocompatible in the short term but also stimulate pre-osteoblast metabolic activity to a greater extent than the reference alloy. Additionally, no significant differences were observed among the HEA samples themselves. The enhanced metabolic activity observed for all HEA samples, with a highly significant increase ($^*p < 0.0001$) compared with the control, suggests a strong stimulatory effect on pre-osteoblast cells. This effect may be associated with the controlled release of bioactive ions such as Mn, Fe, and Al from the HEA samples, which, at appropriate concentrations, can promote osteoblast proliferation and differentiation. Although the reference alloy also stimulated metabolic activity ($p < 0.05$), the superior response elicited by the HEAs highlights their potential to actively modulate cellular behavior. Nevertheless, further studies are required to evaluate the ion release profiles, long-term effects on cell function, and the underlying molecular mechanisms, as well as to confirm the absence of cytotoxic effects in more complex biological models.

Expected performance in biomedical applications

Considering the properties required for biomedical applications, particularly orthopedic applications in bone fixation devices, we, in this section, aim to comparatively evaluate the performance of the HEAs developed in this study with those of the reference alloy and commercially used metallic biomaterials such as CP-Ti grade 2, Ti-64 alloy, Co–Cr alloy, and SS316L. The detailed

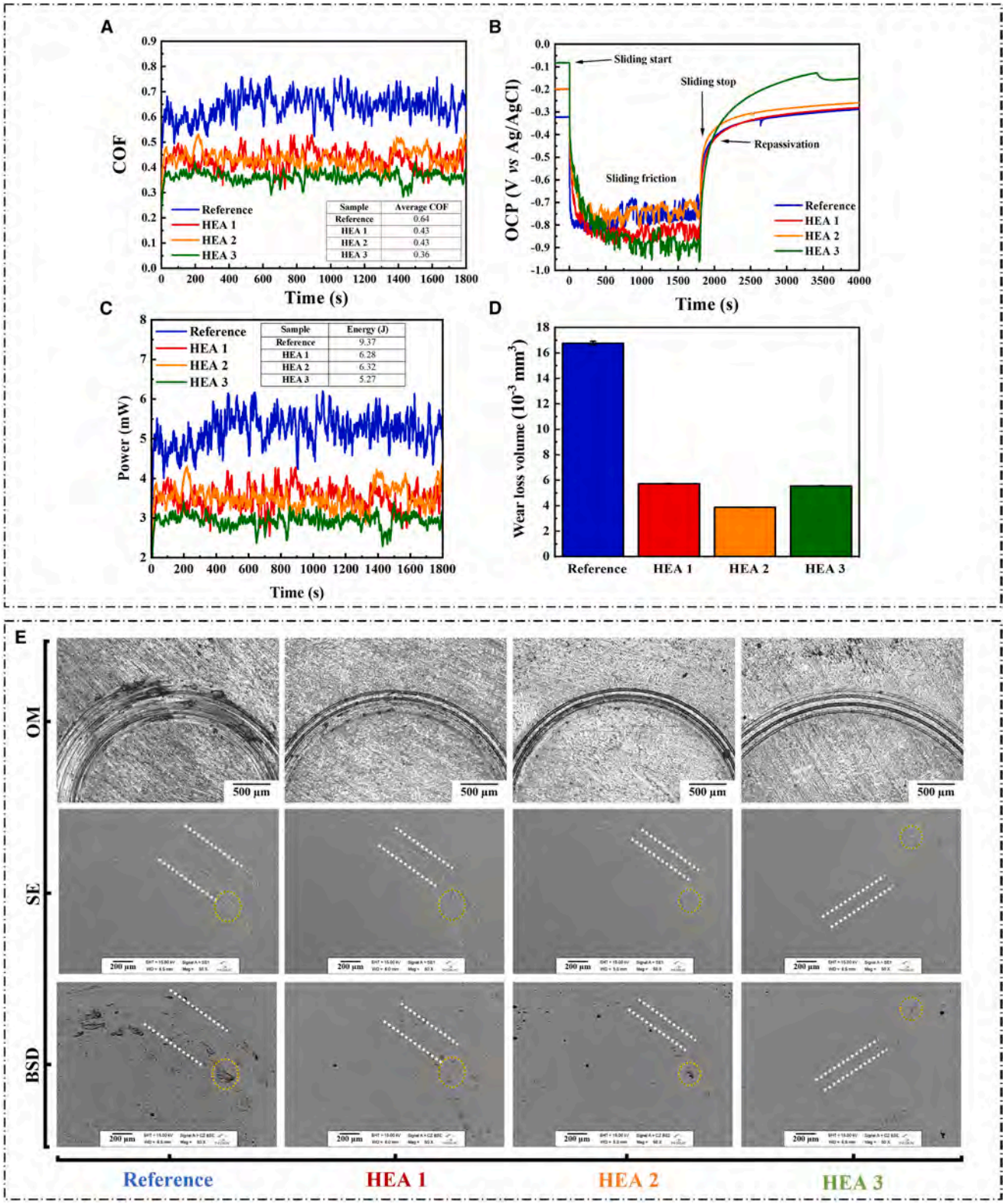


Figure 8. Tribocorrosion tests

(A–E) COF (A), OCP (B), power values over time (C), wear loss volume (D), and micrographs of wear tracks acquired by OM and SEM (E) (scale bars: 200 μm). Grooves and adhered layers are shown in white and orange dashed lines, respectively. Error bars represent the standard deviation (n = 3).

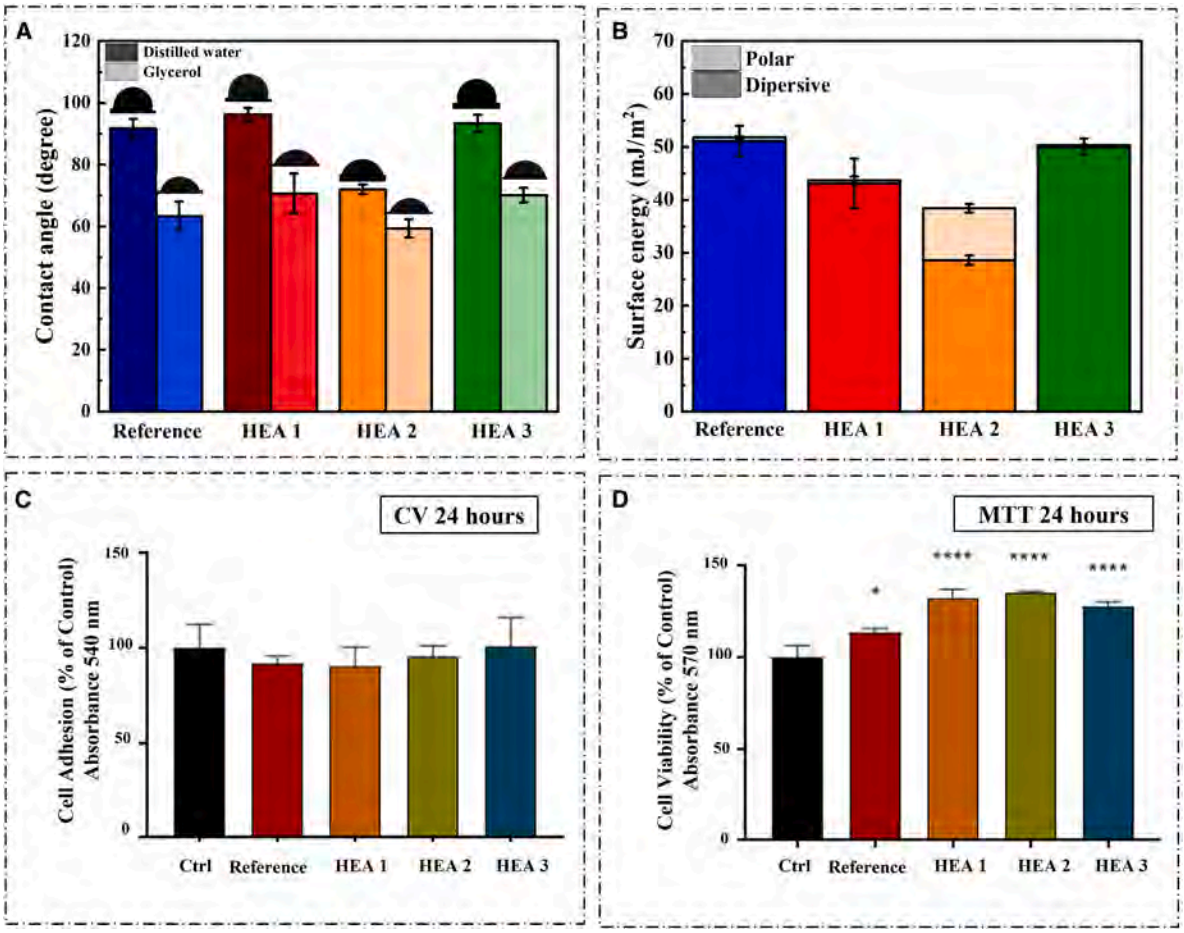


Figure 9. Wettability and cytocompatibility

(A and B) Contact angle values measured in distilled water and glycerol (A), and the corresponding surface free energy values (B). Error bars represent the standard deviation (n = 4). *In vitro* preliminary cytocompatibility assays of the samples after 24 h of exposure using MC3T3-E1 pre-osteoblastic cells.

(C) Cell adhesion evaluated by crystal violet (CV) staining.

(D) Cell viability assessed by MTT assay.

Data are expressed as the mean ± SD (n = 6). *p < 0.05 (reference vs. control) and ****p < 0.0001 (HEA samples vs. control) (one-way ANOVA, Tukey).

values considered for comparison in the graphs presented below are provided in Table S3.

Figure 10A presents the relationship between the estimated cost and melting temperature for metallic biomaterials. The estimated alloy cost was calculated using a rule-of-mixtures approach, in which the contribution of each element was weighted by its mass fraction and corresponding cost, as reported by Sidhu et al.[52] This methodology provides a first-order estimate of the raw-material cost and has been widely used for a comparative assessment of biomedical multicomponent alloys. The commercial materials were also estimated using the same methodology, assuming production from pure elements at the laboratory scale, to enable a preliminary and consistent comparison. The melting temperatures of the alloys were estimated using a rule-of-mixtures approach, calculated as the weighted average of the constituent elements' melting temperatures, based on their respective weight fractions. Based on the data obtained, the HEAs developed in this study exhibit cost values comparable to those of Ti–64 and lower than those estimated for the reference alloy and the commercial Co–Cr alloy. Furthermore, the melting temperatures of the HEAs are among the lowest relative to SS316L stainless steel and the Co–Cr alloy. This factor may further reduce production costs, as lower melting temperatures facilitate processing and reduce the energy required for melting and manufacturing.

Figure 10B presents the relationship between the microhardness-to-elastic modulus ratio (H/E ratio) and the density for metallic biomaterials. The H/E ratio represents the material's elastic strain tolerance, reflecting its ability to withstand elastic deformation before plastic deformation begins. This parameter can indicate the resistance to surface damage and wear under contact loading. In orthopedic applications, a higher H/E ratio is particularly desirable, as it is associated with improved resistance to mechanical degradation, reduced wear particle generation, and enhanced durability under cyclic loading conditions typical of bone fixation devices and joint prostheses. According

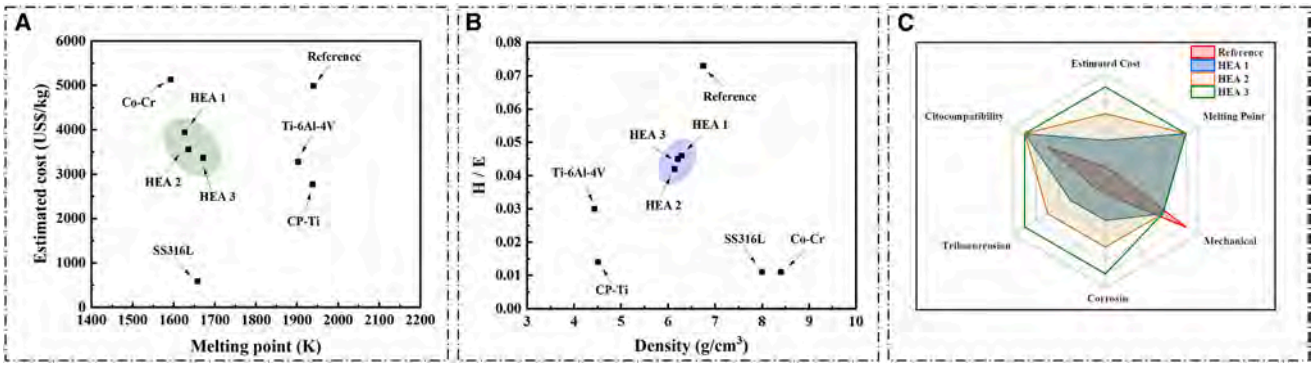


Figure 10. Comparative performance of the samples for the target application

(A) Estimated cost vs. melting point.

(B) H/E ratio vs. density.

(C) Radar map of the overall aspects.

to the graph, the HEAs developed in this study exhibit higher H/E ratios than the commercial biomaterials, surpassing only the reference. This result arises from the combination of a moderate elastic modulus and sufficiently high microhardness, indicating a well-balanced mechanical performance. This finding is consistent with recent studies showing that, although some HEAs do not exhibit a very low elastic modulus, their mechanical strength and elongation are significantly higher than those of conventional biomedical Ti alloys. Regarding the density, although the values were nearly twice those of biomedical CP-Ti and Ti-64 alloys, they remained lower than those of SS316L and Co–Cr alloys. This is a promising result, given the report by Chen et al. [60], which emphasized the importance of lightweight implants in reducing implant weight and minimizing patient discomfort during daily activities. The combination of a high H/E ratio and moderate density enables the development of lightweight implants with improved mechanical compatibility.

Figure 10C presents a radar map constructed using a semi-quantitative scoring system, in which each evaluated parameter was assigned a score from 0 to 3, with 0 indicating the least favorable performance and 3 the most favorable. This analysis aims to provide a global comparison of the properties for the HEAs and the reference, offering a qualitative visualization of the balance among the evaluated properties. Because the radar map is based on the normalized semi-quantitative scores, it should be interpreted only as a qualitative visualization tool and not as an absolute ranking of biomaterial performance. In this analysis, the following parameters were considered: estimated cost; melting temperature; mechanical performance based on the H/E ratio; corrosion behavior by the resistance of the passive oxide film (R_{ox}); tribocorrosion response based on COF and wear loss volume results; and cytocompatibility based on preliminary average results from the MTT and CV assays. The established scoring values are provided in Table S4. According to the projected performance of the samples, the reference stands out in mechanical performance, as expected, because it was selected as the baseline material for this characteristic. However, the HEAs developed in this study exhibited a more balanced distribution of performance across the other evaluated parameters. In particular, HEA 3 exhibited the most balanced distribution of the evaluated properties, among the investigated alloys, for biomedical applications. Given these results, HEA 3 is a strong candidate for further investigation and validation through more in-depth characterization, including tensile testing, fatigue testing, and *in vivo* experiments, which are essential for materials intended for orthopedic applications.

Overall, the developed TiZrNb-based HEAs demonstrate that incorporating the low-cost and non-refractory elements Fe, Mn, and Al provides a viable strategy for obtaining metallic biomaterials with balanced multifunctional properties. The alloys exhibit lower densities than the reference alloy and predominantly consist of a TiNb-rich BCC phase and a ZrFeMnAl-rich C14 Laves phase within chemically segregated dendritic microstructures. The BCC phase undergoes continuous temperature-dependent lattice expansion, while remaining structurally stable over the investigated temperature range, and the interface between the BCC and C14 phases displays a probable semi-coherent character. The combined effect of elemental partitioning, chemical bonding, lattice distortion, and secondary-phase precipitation provides a favorable balance between Vickers microhardness and elastic modulus. The alloys also exhibit slightly hydrophilic surfaces and form stable protective passive films. Their resistance to the combined effect of wear and corrosion surpasses that of the reference alloy, while preliminary *in vitro* assays indicate no cytotoxic effects after 24 h. Although HEA 1 exhibits the lowest elastic modulus and HEA 2 the lowest wear-loss volume, HEA 3 provides the most favorable overall balance of cost, processing feasibility, mechanical performance, electrochemical behavior, tribocorrosion resistance, and short-term cytocompatibility. These findings highlight HEA 3 as the most promising composition for future orthopedic applications. Nevertheless, additional mechanical, electrochemical, and long-term biological investigations are required to confirm its suitability for clinical use.

METHODS

Sample design

For the HEA design, $Ti_{50}Zr_{30}Nb_{10}Ta_{10}$ (atom %) was used as the reference, as it has the lowest elastic modulus (~40 GPa), as

Table 5. Nomenclature and chemical composition of the samples

Composition wt % (atom %)	Reference $Ti_{50}Zr_{30}Nb_{10}Ta_{10}$	HEA 1 $Ti_{44}Zr_{26}Nb_{13}Ta_3Fe_6Mn_4Al_4$	HEA 2 $Ti_{42}Zr_{26}Nb_{16}Fe_6Mn_6Al_4$	HEA 3 $Ti_{42}Zr_{22}Nb_{20}Fe_6Mn_6Al_4$
Ti	30.5 (50.0)	30.5 (43.7)	30.5 (42.4)	30.5 (42.4)
Zr	35.0 (30.1)	35.0 (26.3)	35.0 (25.5)	30.0 (21.9)
Nb	12.0 (10.1)	18.0 (13.3)	23.0 (16.5)	28.0 (20.0)
Ta	22.5 (9.8)	6.5 (2.5)	–	–
Fe	–	5.0 (6.1)	5.0 (6.0)	5.0 (6.0)
Mn	–	3.5 (4.4)	5.0 (6.0)	5.0 (6.1)
Al	–	1.5 (3.8)	1.5 (3.7)	1.5 (3.7)
Chemical aspect	= Ta = Nb × light metals	↓ Ta ↑ Nb + light metals	× Ta ↑ Nb ↑ light metals	↓ Zr ↑ Nb = light metals

indicated in the bond order (Bo)-d-orbital energy level (Md) diagram (Figure S7), making it a suitable benchmark for biomedical applications.[26] The chemical composition of the sample named HEA 1 was designed by replacing some amount of Ta with Nb, Fe, Al, and Mn. Then, HEA 2 was defined by replacing the residual Ta with Nb and Mn, while keeping the non-refractory elements unchanged. Lastly, HEA 3 was proposed by replacing some Zr with Nb to stabilize the BCC crystal structure and maintain the expected elastic modulus. The contents of Fe, Mn, and Al were intentionally limited to avoid excessive precipitation of brittle intermetallic phases. The corresponding chemical details and nomenclature of the samples are presented in Table 5.

Sample processing

Ingots (~60 g) of each sample were produced from commercially pure raw metals (purity >99%). The raw metals were ultrasonically cleaned and weighed at the corresponding nominal concentration, then melted in an argon arc-melting furnace using a water-cooled copper crucible and a tungsten electrode. To ensure an adequate mixture of the alloying elements in solid solution and avoid Mn evaporation (boiling point ~2,334 K), the ingots were melted in two steps: firstly, by mixing elements with relatively low melting points (Ti, Fe, Al, and Mn), and after that, adding the other elements (Zr, Nb, and Ta). For each step, the ingots were remelted at least 5 times to ensure successful mixing. Lastly, a heat treatment was carried out to promote microstructural homogenization under a vacuum of 10^{-5} Pa, with a temperature plateau at 1,273 K for 12 h, followed by slow furnace cooling.

Sample characterization

Density measurements were made using Archimedes' principle with a digital balance and distilled water and compared with theoretical values calculated from the average weighted alloying-element concentrations. The overall chemical analysis was performed using EDXRF (EDX-7200 equipment, Shimadzu Corp., USA). Deionized water and glycerol droplets were used to measure contact angles and estimate the surface energy using Young's equation. Images were taken using a RoHS digital microscope and HiView software version 3.5.72.0. Fiji ImageJ version 1.54p was used to measure the contact angles at both sides of the droplet.

The phase composition was verified by XRD measurements (D/Max 2100/PC Powder X-ray diffractometer, Rigaku Corp., USA), using the powder method, with monochromatic CuK_α radiation (λ = 0.1544 nm), at 40 kV and 20 mA, with a step size of 0.02° and a collecting time of 1.6 s. The XRD profiles were analyzed using the Rietveld method with general structure analysis system[53] (GSAS) and its graphical user interface, EXPGUI.[54] A standard Y_2O_3 sample was used to remove instrumental contributions, and reference crystallographic information files (CIFs) were obtained from the Crystallography Open Database (COD). *In situ* energy-dispersive XRD (EDXRD) experiments were conducted with an EDXRD apparatus comprising a W-anode X-ray tube, an EG&G high-purity Germanium photodiode, and a custom high-temperature cell with a dome-shaped window transparent to X rays. The EDXRD patterns were collected at 50 keV and 30 mA and over a temperature range from room temperature (~300 K) to 773 K. All EDXRD patterns were collected as diffracted intensity as a function of scattering parameter (q) and converted to intensity vs. 2θ for clarity and a more direct comparison with XRD results. The q-scan was conducted spectroscopically, and each EDXRD spectrum was collected in a steady-state configuration without mechanical movement. This feature enables rapid collection of EDXRD patterns with *in situ* monitoring of transient systems (due to temperature variations, chemical reactions, etc.). Further experimental details can be found in our previous studies.[55–57] The cell parameters were obtained from Bragg's law and were temperature dependent. The obtained parameters were fitted using a second-order polynomial function ($f(T) = A \cdot T + B \cdot T^2$), where A and B are the linear and non-linear coefficients, respectively. Then, the functions were used to calculate the CTE of the samples, as indicated by Equations 1 and 2:

$$\textit{Linear CTE} = \frac{1}{x}\left(\frac{\partial x}{\partial T}\right) \text{ and} \qquad \text{(Equation 1)}$$

$$\textit{Volume CTE} = \frac{1}{V}\left(\frac{\partial V}{\partial T}\right), \qquad \text{(Equation 2)}$$

where x denotes the cell parameters (a) for the BCC phase, V is the cell volume, and T is the temperature.

For microstructural analyses, the samples were previously sectioned using a precision cutting machine and then subjected

to a standard metallographic procedure of grinding with waterproof SiC papers (#180 to #1500 mesh), polishing (0.25 μm; Al_2O_3 suspension), and etching (aqueous HF and HNO_3 solutions). Microstructural analysis was performed using OM (BX51M microscope, Olympus Corp., USA) and SEM (EVO LS15 microscope, Carl Zeiss Inc., USA), with secondary electron (SE) and BSD electron imaging modes. Specific details at the sub-micrometric scale were evaluated by scanning transmission electron microscopy (STEM; Titan Themis, FEI Inc., USA) at 300 kV. The SAED indexing was performed with CrysTBox version 1.10, using the same CIF files used in the Rietveld refinement, while the FFT of HRTEM images was analyzed using Fiji ImageJ software. For TEM analysis, a sample lamella was prepared using an FIB system coupled with an SEM equipment (Thermo Fisher Scientific, Helios NanoLab 660, USA).

Sample testing

Mechanical properties were evaluated using Vickers microhardness (HMV-G microdurometer, Shimadzu Corp., USA) at a load of 0.3 kgf (2.942 N) and a dwell time of 15 s, and elastic modulus measurements were performed with the impulse excitation method (Sonelastic equipment, ATCP Physical Engineering Corp., Brazil), using rectangular specimens (22 × 4 × 1 mm).

Electrochemical experiments were conducted in individual 250 mL glass electrochemical cells, each containing approximately 200 mL of aerated PBS at 293 ± 1 K. The nominal composition of PBS (Sigma-Aldrich) is: 137 mM NaCl, 2.7 mM KCl, 10 mM Na_2HPO_4, and 1.8 mM KH_2PO_4. The tests used a conventional three-electrode configuration, comprising the samples as the working electrode (WE), a saturated KCl Ag/AgCl RE (E = +0.197 V vs. SHE; Gamry Skinny Reference Electrode, model 932-00018), and a platinum mesh counter electrode (CE). The RE was positioned as close as possible to the WE to minimize solution resistance, thereby eliminating the need for iR compensation. Electrochemical analyses were performed in duplicate using a Gamry potentiostat/galvanostat (Interface 1010) in a conventional three-electrode cell configuration. Anodic polarization curves were obtained from two replicate samples after stabilization of the OCP had been confirmed. Measurements were conducted under quasi-stationary conditions starting from a potential of −0.2 V vs. OCP to 1.5 V vs. Ag/AgCl (sat. KCl) at a scan rate of 10 $mV \cdot min^{-1}$ (0.166 $mV \cdot s^{-1}$). EIS measurements were carried out by applying a sinusoidal perturbation of ±10 mV with respect to the OCP over a frequency range from 100 kHz to 0.01 Hz, with a resolution of 10 points per decade. All electrochemical data were normalized to the exposed surface area of the samples, which ranged from 2.3 to 4.3 cm^2. Surface morphology and composition of the samples after anodic polarization were determined using SEM/EDS (JEOL JED-2300, 15kV).

For the tribocorrosion test, the samples (WE) were mounted in an electrochemical cell with a saturated Ag/AgCl electrode (RE). Subsequently, the electrochemical cells were mounted in a pin-on-disk tribometer for reciprocating motion. Friction was applied using an alumina ball (ϕ = 6 mm). OCP values were recorded before, during, and after sliding by using a potentiostat (model 34401A, Agilent Inc., USA). The test parameters included a normal load (N) of 2 N, a 2-mm radius circular wear track (r), a rotational speed (ω) of 2 $rad \cdot s^{-1}$ (0.32 Hz), and a sliding time of 30 min. HBSS (Hank's Balanced Salt Solution) was used as the electrolyte, and the tests were conducted at body temperature (~310 K). The transferred energy (E) into the samples during sliding was estimated using the equation $E = \int P(t) \cdot dt$, where P(t) is the instantaneous power acquired in the tests. Power values were obtained from the relation $P(t) = F_{friction}(t) \cdot \omega r$, where $F_{friction}(t) = COF(t) \cdot N$ is the instantaneous coefficient of friction value, and $v = \omega r$ is the collected speed during the sliding. Later, the wear track was examined by OM and SEM. The wear loss volume was estimated by: $V = 2\pi r \cdot A$, where r is the radius of the circular wear track (2 mm), and A is the removed area calculated from optical profilometry measurements (Dektak 150 profilometer, Veeco Metrology, USA), using a stylus radius of 12.5 μm, a scan length of 2000 μm, a resolution of 0.16 μm, over 20 s, and an applied load of 3 mgf. The average values were obtained by examining the wear tracks of two samples per group after the tribocorrosion tests.

The preliminary biological assays were conducted using MC3T3-E1 (subclone 4), mouse pre-osteoblastic cells (ATCC CRL-2593), which were cultured in α-minimum essential medium (α-MEM) supplemented with 10% fetal bovine serum (FBS) at 310 K and 5% CO_2. Sub-confluent passages were trypsinized and used in all experiments. The MTT assay was used to assess *in vitro* cytocompatibility. Briefly, pre-osteoblasts were seeded in 96-well plates at a density of 1 × 10^4 cells per well and exposed to media previously conditioned with the samples (0.2 $g \cdot mL^{-1}$ for 24 h).[15,58] After 24 h of treatment, the medium was removed and replaced with 100 μL of MTT solution (3-(4,5-dimethylthiazol-2-yl)-2,5-diphenyltetrazolium bromide, 1 $mg \cdot mL^{-1}$ in α-MEM without FBS). Following 3 h of incubation at 310 K, the MTT solution was aspirated, and the precipitated formazan was solubilized in 100 μL of absolute ethanol. Absorbance was measured at 570 nm using a SYNERGY-HTX microplate reader (Biotek, USA).[58] Cell adhesion was evaluated using the CV assay; the cells were trypsinized and seeded at a density of 1 × 10^4 cells per well in 96-well plates, using the same conditioned media described above. A control group cultured in conventional α-MEM (without exposure to materials) was included for comparison. After 24 h of incubation, the cells were stained with CV, and cell adhesion was quantified by measuring dye incorporation using a previously described method. Absorbance was measured at 540 nm (SYNERGY-HTX, Biotek, USA). For both assays, six replicates were used per group (n = 6). Data are expressed as the mean ± standard deviation (SD). Statistical analyses were performed using GraphPad Prism 7 (GraphPad Software, USA). One-way ANOVA followed by Tukey's post hoc test was used, and a p value <0.05 was considered significant for all tests.

RESOURCE AVAILABILITY

Lead contact

Requests for further information and resources should be directed to and will be fulfilled by the lead contact, Jhuliene E.M. Torrento (jhuliene.torrento@unesp.br).

Materials availability

This study did not generate new, unique reagents.

Data and code availability

- The data reported in this paper will be shared by the lead contact upon request.
- This paper does not report original code.
- Any additional information required to reanalyze the data reported in this paper is available from the lead contact upon request.

ACKNOWLEDGMENTS

The authors acknowledge the researchers Dr. M.L. Lourenço and Prof. Dr. J.E. Spinelli from DEMa, UFSCar – São Carlos, for the EDS and wettability analyses, respectively, and Dr. C.A.O. Ramirez from LNNano, CNPEM – Campinas, for the TEM analysis. The authors also thank LNNano for the FIB preparation and TEM analysis (Proposal #20233406). This study was supported by the Brazilian funding agencies: São Paulo Research Foundation (FAPESP; grants #2021/13921-3, #2023/15812-2, #2024/01132-2, #2024/03886-4, and #2024/03148–3), National Council for Scientific and Technological Research (CNPq; grants #314.810/2021-8, #404020/2023–2, #421.677/2023-6, #408594/2024-1, #304400/2025-4, and #312391/2025-0), and Coordination of Superior Level Staff Improvement (CAPES; grants #88887.890647/2023-00, #88887.898681/2023-00, and #88887.976789/2024–00).

AUTHOR CONTRIBUTIONS

Conceptualization, D.R.N.C.; methodology, D.R.N.C.; data curation, J.E.M.T., T.d.S.P.d.S., C.R.M.A., C.A.F.P., G.S.d.A., W.F.Z., M.R.C., M.F., J.V.R., S.S., G.U., and G.G.; investigation, J.E.M.T., T.d.S.P.d.S., C.R.M.A., C.A.F.P., G.S.d.A., W.F.Z., M.R.C., M.F., J.V.R., S.S., G.U., and G.G.; writing – original draft, J.E.M.T.; writing – review & editing, D.R.N.C. and C.R.G.; supervision, D.R.N.C.; and funding acquisition, D.R.N.C. and C.R.G.

DECLARATION OF INTERESTS

The authors declare that they have no known competing financial interests or personal relationships that could have influenced the work reported in this paper.

SUPPLEMENTAL INFORMATION

Supplemental information can be found online at https://doi.org/10.1016/j.xcrp.2026.103547.

Received: May 25, 2026
Revised: July 21, 2026
Accepted: August 24, 2026
Published: September 11, 2026

REFERENCES

1. Prasad, K., Bazaka, O., Chua, M., Rochford, M., Fedrick, L., Spoor, J., Symes, R., Tieppo, M., Collins, C., Cao, A., et al. (2017). Metallic biomaterials: Current challenges and opportunities. Materials *10*, 884. https://doi.org/10.3390/ma10080884.
2. Kaur, M., and Singh, K. (2019). Review on titanium and titanium based alloys as biomaterials for orthopaedic applications. Mater. Sci. Eng. C Mater. Biol. Appl. *102*, 844–862. https://doi.org/10.1016/j.msec.2019.04.064.
3. Castro, D., Jaeger, P., Baptista, A.C., and Oliveira, J.P. (2021). An Overview of High-Entropy Alloys as Biomaterials. Metals *11*, 648. https://doi.org/10.3390/met11040648.
4. Chen, C.-L.; Suprianto (2020). Microstructure and mechanical properties of AlCuNiFeCr high entropy alloy coatings by mechanical alloying. Surf. Coat. Technol. *386*, 125443. https://doi.org/10.1016/j.surfcoat.2020.125443.
5. Avila-Rubio, M.A., Baldenebro-Lopez, J.A., Soto-Rojo, R., Ceballos-Mendivil, L.G., Carreño, G., Garza-Montes-de-Oca, N.F., and Baldenebro-Lopez, F.J. (2020). Effect of Mo and Ti on the microstructure and microhardness in AlCoFeNiMoTi high entropy alloys prepared by mechanical alloying and conventional sintering. Adv. Powder Technol. *31*, 1693–1701. https://doi.org/10.1016/j.apt.2020.02.008.
6. Mooraj, S., and Chen, W. (2023). A review on high-throughput development of high-entropy alloys by combinatorial methods. J. Mater. Inf. *3*, 4. https://doi.org/10.20517/jmi.2022.41.
7. Chen, W., and Li, X. (2024). Structure and mechanical properties of novel lightweight refractory high entropy alloys NbMoTiZr-(Al/V): A combined first principles and experimental study. J. Alloys Compd. *973*, 172855. https://doi.org/10.1016/j.jallcom.2023.172855.
8. Rashidy Ahmady, A., Ekhlasi, A., Nouri, A., Haghbin Nazarpak, M., Gong, P., and Solouk, A. (2023). High entropy alloy coatings for biomedical applications: A review. Smart Materials in Manufacturing *1*, 100009. https://doi.org/10.1016/j.smmf.2022.100009.
9. Ostovari Moghaddam, A., Abdollahzadeh, A., Samodurova, M., Shaburova, N., Mikhailov, D., Fereidonnejad, R., Zhivulin, V., and Trofimov, E. (2022). Novel high entropy intermetallic compounds: Synthesis and detonation spraying. Intermetallics *146*, 107591. https://doi.org/10.1016/j.intermet.2022.107591.
10. Zhang, D., Li, Q., Sun, R., Chang, C., Liu, B., and Ma, X. (2024). Effect of Mn addition on microstructure and corrosion behavior of AlCoCrFeNi high-entropy alloy. Intermetallics *167*, 108236. https://doi.org/10.1016/j.intermet.2024.108236.
11. Shafiei, A., Khani Moghanaki, S., and Amirjan, M. (2023). Effect of heat treatment on the microstructure and mechanical properties of a dual phase Al14Co41Cr15Fe10Ni20 high entropy alloy. J. Mater. Res. Technol. *26*, 2419–2431. https://doi.org/10.1016/j.jmrt.2023.08.071.
12. Asta, M., Beckermann, C., Karma, A., Kurz, W., Napolitano, R., Plapp, M., Purdy, G., Rappaz, M., and Trivedi, R. (2009). Solidification microstructures and solid-state parallels: Recent developments, future directions. Acta Mater. *57*, 941–971. https://doi.org/10.1016/j.actamat.2008.10.020.
13. Osório, W.R., Freire, C.M., and Garcia, A. (2005). The effect of the dendritic microstructure on the corrosion resistance of Zn–Al alloys. J. Alloys Compd. *397*, 179–191. https://doi.org/10.1016/j.jallcom.2005.01.035.
14. Guo, Y., He, J., Li, Z., Wu, X., Lu, W., and Liu, C. (2022). Solidification segregation-driven microstructural evolution of trace yttrium-alloyed TaMoNbZrTiAl refractory high entropy alloys. Mater. Charact. *194*, 112495. https://doi.org/10.1016/j.matchar.2022.112495.
15. Torrento, J.E., Sousa, T.d.S.P.d., Cristino da Cruz, N., Santos de Almeida, G., Zambuzzi, W.F., Grandini, C.R., and Nespeque Correa, D.R. (2022). Development of non-equiatomic Bio-HEAs based on TiZrNbTa-(Mo and Mn). APL Mater. *10*, 081113. https://doi.org/10.1063/5.0100465.
16. Hua, N., Wang, W., Wang, Q., Ye, Y., Lin, S., Zhang, L., Guo, Q., Brechtl, J., and Liaw, P.K. (2021). Mechanical, corrosion, and wear properties of biomedical Ti–Zr–Nb–Ta–Mo high entropy alloys. J. Alloys Compd. *861*, 157997. https://doi.org/10.1016/j.jallcom.2020.157997.
17. Xiong, W., Guo, A.X.Y., Zhan, S., Liu, C.-T., and Cao, S.C. (2023). Refractory high-entropy alloys: A focused review of preparation methods and properties. J. Mater. Sci. Technol. *142*, 196–215. https://doi.org/10.1016/j.jmst.2022.08.046.
18. Gurel, S., Nazarahari, A., Canadinc, D., Cabuk, H., and Bal, B. (2021). Assessment of biocompatibility of novel TiTaHf-based high entropy alloys for utility in orthopedic implants. Mater. Chem. Phys. *266*, 124573. https://doi.org/10.1016/j.matchemphys.2021.124573.
19. Wong, K.-K., Hsu, H.-C., Wu, S.-C., Hung, T.-L., and Ho, W.-F. (2022). Structure, Properties, and Corrosion Behavior of Ti-Rich TiZrNbTa Medium-Entropy Alloys with $\beta+\alpha''+\alpha'$ for Biomedical Application. Materials *15*, 7953. https://doi.org/10.3390/ma15227953.
20. Li, Z., Lai, W., Tong, X., You, D., Li, W., and Wang, X. (2022). Design of TiZrNbTa multi-principal element alloys with outstanding mechanical properties and wear resistance. Materials Science and Engineering: A *845*, 143203. https://doi.org/10.1016/j.msea.2022.143203.
21. Chen, J., Ma, F., Liu, P., Wang, C., Liu, X., Li, W., and Han, Q. (2019). Effects of Nb on Superelasticity and Low Modulus Properties of Metastable

β-Type Ti-Nb-Ta-Zr Biomedical Alloys. J. Mater. Eng. Perform. *28*, 1410–1418. https://doi.org/10.1007/s11665-019-03897-4.

22. Senopati, G., Rahman Rashid, R.A., Kartika, I., and Palanisamy, S. (2023). Recent Development of Low-Cost β-Ti Alloys for Biomedical Applications: A Review. Metals *13*, 194. https://doi.org/10.3390/met13020194.
23. Oh, J.M., Park, C.H., Yeom, J.-T., Hong, J.-K., Kang, N., and Lee, S.W. (2020). High strength and ductility in low-cost Ti–Al–Fe–Mn alloy exhibiting transformation-induced plasticity. Materials Science and Engineering: A *772*, 138813. https://doi.org/10.1016/j.msea.2019.138813.
24. Balaji, V., and Anthony Xavior, M.A. (2024). Development of high entropy alloys (HEAs): Current trends. Heliyon *10*, e26464. https://doi.org/10.1016/j.heliyon.2024.e26464.
25. Andersson, J.O., Helander, T., Höglund, L., Shi, P., and Sundman, B. (2002). Thermo-Calc & DICTRA, computational tools for materials science. Calphad *26*, 273–312. https://doi.org/10.1016/S0364-5916(02)00037-8.
26. Abdel-Hady, M., Hinoshita, K., and Morinaga, M. (2006). General approach to phase stability and elastic properties of β-type Ti-alloys using electronic parameters. Scr. Mater. *55*, 477–480. https://doi.org/10.1016/j.scriptamat.2006.04.022.
27. Xu, Y., Li, C., Huang, Z., Chen, Y., and Zhu, L. (2020). Microstructure Evolution and Mechanical Properties of FeCoCrNiCuTi0.8 High-Entropy Alloy Prepared by Directional Solidification. Entropy *22*, 786. https://doi.org/10.3390/e22070786.
28. Xu, G., Zhao, X., Xia, W., Yue, Q., Zheng, Z., Gu, Y., and Zhang, Z. (2025). A review on microstructure design, processing, and strengthening mechanism of high-strength titanium alloys. Prog. Nat. Sci. Mater. Int. *35*, 258–277. https://doi.org/10.1016/j.pnsc.2025.01.005.
29. Samsonov, G.V. (1968). Atomic Structure and Crystallochemical Properties of the Elements. In Handbook of the Physicochemical Properties of the Elements, G.V. Samsonov, ed. (Springer US), pp. 7–130. https://doi.org/10.1007/978-1-4684-6066-7_2.
30. Mishra, S.S., Yadav, T.P., Srivastava, O.N., Mukhopadhyay, N.K., and Biswas, K. (2020). Formation and stability of C14 type Laves phase in multi component high-entropy alloys. J. Alloys Compd. *832*, 153764. https://doi.org/10.1016/j.jallcom.2020.153764.
31. Lide, D.R. (2007). Handbook of Chemistry and Physics. CRC Handbook of Chemistry and Physics, 88th ed. (CRC Press)), pp. 1–2640.
32. da Silva Bezerra, A., Ribeiro, A.K.C., Veríssimo, A.H., and de Almeida, E.O. (2025). Prosthetic complications and failures of implant-supported fixed partial dentures: A scoping review. J. Prosthet. Dent *134*, 643–650. https://doi.org/10.1016/j.prosdent.2023.10.025.
33. Chen, W., and Zhang, H. (2023). An experimental study on the impact of prosthesis temperature on the biomechanical properties of bone cement fixation. BMC Surg. *23*, 191. https://doi.org/10.1186/s12893-023-02079-3.
34. Sousa, T.S.P., Torrento, J.E.M., Kuroda, P.A.B., Gonçalves, V.R.M., Coan, K.S., Correa, D.R.N., and Grandini, C.R. (2024). Surface aspects of novel Bio-HEAs MAO-treated in a Ca-P-and Mg-rich electrolyte. Appl. Surf. Sci. *664*, 160227. https://doi.org/10.1016/j.apsusc.2024.160227.
35. Rajabi, M., Dehghani, K., and Shahmir, H. (2024). Development of a novel Ti35Nb25Zr15Mo15V10 high-entropy alloy for metallic biomaterials. Phys. B Condens. Matter *691*, 416283. https://doi.org/10.1016/j.physb.2024.416283.
36. Iijima, Y., Nagase, T., Matsugaki, A., Wang, P., Ameyama, K., and Nakano, T. (2021). Design and development of Ti–Zr–Hf–Nb–Ta–Mo high-entropy alloys for metallic biomaterials. Mater. Des. *202*, 109548. https://doi.org/10.1016/j.matdes.2021.109548.
37. El Aalami, B., Idrissi, H., and Trabadelo, V. (2026). C14-Laves phase high entropy alloys for hydrogen storage: a review. Mater. Horiz. *13*, 3721–3760. https://doi.org/10.1039/D5MH01719J.
38. Stein, F., and Leineweber, A. (2021). Laves phases: a review of their functional and structural applications and an improved fundamental understanding of stability and properties. J. Mater. Sci. *56*, 5321–5427. https://doi.org/10.1007/s10853-020-05509-2.
39. Hirata, A., and Koyama, Y. (2004). Crystallographic correspondence between the bcc and C14-type structures in the Fe–Ti alloy system. Materials Science and Engineering: A *374*, 72–76. https://doi.org/10.1016/j.msea.2003.12.066.
40. Zhao, Y., Sun, L., Wang, L., Zhang, J., Fang, Y., and Zhan, X. (2025). Synergistic strength-ductility enhancement of AlNbTiVZr lightweight refractory high entropy alloys with regulated Laves distribution morphology: Network-to-dispersion transformation. Materials Science and Engineering: A *927*, 148001. https://doi.org/10.1016/j.msea.2025.148001.
41. Huang, X., Xie, G., Liu, X., Fu, H., Shao, L., and Hao, Z. (2020). The influence of precipitation transformation on Young's modulus and strengthening mechanism of a Cu–Be binary alloy. Materials Science and Engineering: A *772*, 138592. https://doi.org/10.1016/j.msea.2019.138592.
42. Shi, H., Xu, C., Hu, X., Gan, W., Wu, K., and Wang, X. (2022). Improving the Young's modulus of Mg via alloying and compositing – A short review. J. Magnes. Alloy. *10*, 2009–2024. https://doi.org/10.1016/j.jma.2022.07.011.
43. Gorban, V.F., Krapivka, M.O., and Myslyvchenko, O.M. (2024). Properties of equiatomic high-entropy laves phases of laves phase of C14 type. Mater. Sci. *60*, 217–223. https://doi.org/10.1007/s11003-025-00875-1.
44. Wang, S.D., Liu, X.J., Lei, Z.F., Lin, D.Y., Bian, F.G., Yang, C.M., Jiao, M.Y., Du, Q., Wang, H., Wu, Y., et al. (2021). Chemical short-range ordering and its strengthening effect in refractory high-entropy alloys. Phys. Rev. B *103*, 104107. https://doi.org/10.1103/PhysRevB.103.104107.
45. Preda, L., Leau, S.A., Donath, C., Neacsu, E.I., Maxim, M.E., Sătulu, V., Paraschiv, A., and Marcu, M. (2023). Investigation of Long-Term Corrosion of CoCrMoW Alloys under Simulated Physiological Conditions. Metals *13*, 1881. https://doi.org/10.3390/met13111881.
46. Gudić, S., Nagode, A., Šimić, K., Vrsalović, L., and Jozić, S. (2022). Corrosion Behavior of Different Types of Stainless Steel in PBS Solution. Sustainability *14*, 8935. https://doi.org/10.3390/su14148935.
47. Gudić, S., Vrsalović, L., Kvrgić, D., and Nagode, A. (2021). Electrochemical Behaviour of Ti and Ti-6Al-4V Alloy in Phosphate Buffered Saline Solution. Materials *14*, 7495. https://doi.org/10.3390/ma14247495.
48. Komarova, E.G., Sharkeev, Y.P., Sedelnikova, M.B., Prymak, O., Epple, M., Litvinova, L.S., Shupletsova, V.V., Malashchenko, V.V., Yurova, K.A., Dzyuman, A.N., et al. (2020). Zn- or Cu-containing CaP-Based Coatings Formed by Micro-Arc Oxidation on Titanium and Ti-40Nb Alloy: Part II—Wettability and Biological Performance. Materials *13*, 4366. https://doi.org/10.3390/ma13194366.
49. Gonçalves, V.R.M., Cardoso, G.C., de Freitas Quadros, F., Corrêa, D.R.N., Pintão, C.A.F., Afonso, C.R.M., Lisboa Filho, P.N., and Grandini, C.R. (2025). Effects of α- and β-Ti phases as unreinforced or TiC-reinforced substrates on plasma electrolytic oxidation coatings for biomedical use. Surf. Coat. Technol. *518*, 132878. https://doi.org/10.1016/j.surfcoat.2025.132878.
50. Barberi, J., and Spriano, S. (2021). Titanium and Protein Adsorption: An Overview of Mechanisms and Effects of Surface Features. Materials *14*, 1590. https://doi.org/10.3390/ma14071590.
51. ISO10993-5, I.O.f.S. (1999). Biological evaluation of medical devices. Part 5: Tests for cytotoxicity: in vitro methods. International Organization for Standardization. ISO 10993-5: Biological Evaluation of Medical Devices - Part 5: Tests for in Vitro Cytotoxicity (International Organization for Standardization).
52. Sidhu, S.S., Singh, H., and Gepreel, M.A.-H. (2021). A review on alloy design, biological response, and strengthening of β-titanium alloys as biomaterials. Mater. Sci. Eng. C Mater. Biol. Appl. *121*, 111661. https://doi.org/10.1016/j.msec.2020.111661.
53. Toby, B.H., and Von Dreele, R.B. (2013). GSAS-II: the genesis of a modern open-source all purpose crystallography software package. J. Appl. Crystallogr. *46*, 544–549. https://doi.org/10.1107/S0021889813003531.
54. TOBY, B.H. (2001). EXPGUI, a Graphical User Interface for GSAS. J. Appl. Crystallogr. *34*, 210–213. https://doi.org/10.1107/s0021889801002242.

55. Rau, J.V., Generosi, A., Smirnov, V.V., Ferro, D., Rossi Albertini, V., and Barinov, S.M. (2008). Energy dispersive X-ray diffraction study of phase development during hardening of calcium phosphate bone cements with addition of chitosan. Acta Biomater. *4*, 1089–1094. https://doi.org/10.1016/j.actbio.2008.01.006.

56. Rau, J.V., Fosca, M., Komlev, V.S., Fadeeva, I.V., Rossi Albertini, V., and Barinov, S.M. (2010). In Situ Time-Resolved Studies of Octacalcium Phosphate and Dicalcium Phosphate Dihydrate in Simulated Body Fluid: Cooperative Interactions and Nanoapatite Crystal Growth. Cryst. Growth Des. *10*, 3824–3834. https://doi.org/10.1021/cg100746a.

57. Graziani, V., Fosca, M., Egorov, A.A., Zobkov, Y.V., Fedotov, A.Y., Baranchikov, A.E., Ortenzi, M., Caminiti, R., Komlev, V.S., and Rau, J.V. (2016). Zinc-releasing calcium phosphate cements for bone substitute materials. Ceram. Int. *42*, 17310–17316. https://doi.org/10.1016/j.ceramint.2016.08.027.

58. Almeida, G.S.d., Carra, M.G.J., dos Santos, M.L.P., Bucci, J., Suter, L.C., Corrêa, D.R.N., Chevalier, P., Saeki, M.J., Mantovani, D., and Zambuzzi, W.F. (2026). Optimizing Titanium Osseointegration through Thermally Modified Co-Doped Monetite Coatings. ACS Biomater. Sci. Eng. *12*, 1522–1534. https://doi.org/10.1021/acsbiomaterials.5c01648.